Formation & maintenance of photoreceptor outer segments

Inauguraldissertation
zur
Erlangung der Würde eines Doktors der Philosophie
vorgelegt der
Philosophisch-Naturwissenschaftlichen Fakultät
der Universität Basel
von

Janine Daum
aus München, Deutschland
Basel, 2017

Genehmigt von der Philosophisch-Naturwissenschaftlichen Fakultät

auf Antrag von

Prof. Dr. Susan Gasser (Fakultaetsverantwortliche)

Prof. Dr. Botond Roska (Dissertationsleiter)

Prof. Dr. Stephan Neuhauss (Korefferent)

Basel, den 20.6.2017

Prof. Dr. Martin Spiess

(Dekan der Philosophisch-Naturwissenschaftlichen Fakultät)

Statement

All experiments and data analysis presented in this PhD thesis were performed by Janine Daum. All illustrations shown in this thesis were created by Janine Daum.

The work was carried out at the Friedrich Miescher Institute for Biomedical Research in Basel, Switzerland, under the supervision of Prof. Dr. Botond Roska.

The main project, "Outer segment formation" (Project 1), is based on Janine Daum's unpublished work. The side project, "Outer segment maintenance" (Project 2), is based on work published in Busskamp et al. (2014b).

Nur die Harten komm' in' Garten.

(German saying: Only the tough ones will go to paradise.)

Abstract

High-resolution vision is mediated by cone photoreceptors. The molecular programs responsible for the formation and maintenance of their light sensor, the outer segment, are not well understood.

In my main project, I correlated daily changes in ultrastructure and gene expression in postmitotic mouse cone photoreceptors in the retina, between birth and eye opening, using serial block-face electron microscopy and RNA sequencing. Outer segments appeared rapidly at postnatal day six and their appearance coincided with a switch in gene expression. The switch affected more than 14% of all genes expressed in cones. Genes that switched off were rich in transcription factors and neurogenic genes. Those that switched on contained genes relevant for cone function. Extensive chromatin rearrangements in enhancer regions occurred before the switch but not after. This work shows that the growth of a key compartment of a postmitotic sensory cell involves a rapid and extensive switch in gene expression and chromatin accessibility.

In a side project, my coworkers and me found that miRNAs 182 and 183 are necessary for cone outer segment maintenance in vivo and functional outer segment formation in stem cell derived retinal organoids.

Thank you

Botond Roska, Susan Gasser, Rainer Friedrich, Stephan Neuhauss, Hubertus Kohler, Christel Genoud, Moritz Kischmann, Laurent Gelman, Steve Bourke, Stephane Thiry, Kirsten Jacobeit, Tim Roloff, Sebastian Smallwood, Urs Disler, Kamill Balint, Volki Busskamp, Therese Cronin, Sabrina Djaffer, Tony Drinnenberg, Jens Dübel, Federico Esposti, Karl Farrow, Brigitte Gross, Peter Hantz, Daniel Hillier, Sjoerd Holwerda, Phine Jüttner, Özkan Keles, Jacek Krol, Oliver Krone, Monique Lerch, Emilie Mace, Dasha Nelidova, Rei Morikawa, Tisi Munz, Claudia Patino, Zoli Raics, Santiago Rompani, Michael Stadler, Tamas Szikra, Miguel Texeira, Stuart Trenholm, Adi Wertz, Paula Daum, Inge Hall, Alex Hall, Doro Hall, Ilse Krüger, Ernst Krüger, Alex Attinger, Darko Barisic, Ximena Bonilla, Javier Collin, Leyla Davis, Karin Erni & Co, Alici Färber, Adriana Gonzales, Irina Demina, Omar Jallow, Noinoi Laas, Karen Lavi, Mili Markovic, Fabienne Meier-Abt, Florence Murphey & Co, Robi Ohlendof, Kripa Parshotam & Co, Tom Russell, Jules Schmidt, Debora Schmitz, Andrew Seeber, Constantin Skula, Domi Waldvogel, Jessica Wassermann, Stefan Widmer, Babette Wolf & Co, Stoili Zethner, Chrissi Fasnacht, Keith Guapala, Isabella Marcomini, Cheryl Kunz, Sara Toprak, Peter Zeller, Conny Imhof, Shu-Kun Lin, Didi Rohrdorf, Leo Wyss, Swiss National Science Foundation, Boehringer Ingelheim Fonds

▽

superb supervisor | committed committee | fabulous FMI facilities
clever colleagues | fantastic family | fun friends | super students
outstanding others | supporting scholarships

Contents

1 | Introduction

The nervous system extracts information from the environment via specialized sensory cells, which convert changes in physical quantities such as the number of photons, mechanical pressure, or the concentration of chemicals into neuronal signals. This conversion takes place in dedicated neuronal compartments (Avidor-Reiss et al., 2004). Photons are detected in the outer segments of photoreceptors (Figure 1) in the visual system. Mechanical pressure is detected in the various protrusions of mechanoreceptors in the somatosensory system and in the hair bundles of hair cells in the auditory and vestibular system. Concentration of chemicals is detected in the cilia of the olfactory receptor neurons in the olfactory system. These different biological sensors are especially sensitive to genetic perturbations and are the most frequent sites of sensory loss (Street and Wcn, 2016; Wheway et al., 2014). To prevent or repair sensory loss, it is important to understand how these biological sensors form and how they are maintained. In my thesis, I studied the visual system and asked: How do the light sensors of photoreceptors form in the developing animal and how are they maintained throughout its lifetime?

Image-forming vision is initiated by two types of photoreceptors: rods and cones. They sense light signals and transform them into neuronal signals. Human visual function is particularly dependent on cones, because they function during daylight and are the photoreceptors required for high-resolution vision and color

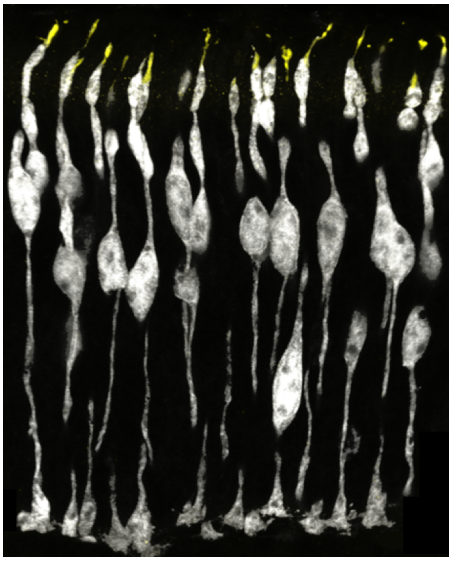

Figure 1. Photoreceptor cells. Confocal microscopy image of the light-sensing outer segments (yellow) of mouse cone photoreceptors (white). A region of $80 \times 90\,\mu m$ is shown.

vision (Sahel and Roska, 2013). Photoreceptors are cells of the retina, which is a neuronal tissue located in the back of the eye. The retina is part of the central nervous system because it not only detects but also processes visual inputs. The retina has a layered structure (Figure 2) consisting of three main glutamatergic excitatory cell types: photoreceptors, bipolar cells, and ganglion cells. Photoreceptors translate the information from light signals into neuronal signals and give input to a diverse population of bipolar cells, which transmit the signals to ganglion cells. Axons of ganglion cells form the optic nerve, which carries preprocessed signals to higher brain areas. The flow of visual information is modulated by two inhibitory cell populations: horizontal cells and amacrine cells. Horizontal cells give negative feedback to photoreceptors and modify the photoreceptor-to-bipolar cell signaling. In addition, a large population of inhibitory amacrine cells modulates the transfer of information between bipolar and ganglion cells (Werblin, 2011).

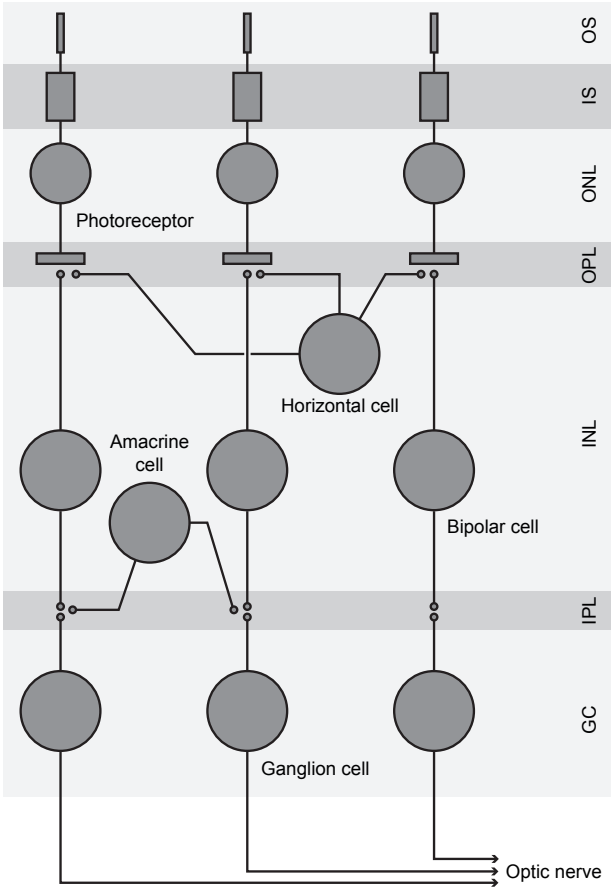

Figure 2. Schematic representation of cellular layers in the retina. The outermost layer is comprised of the photoreceptors' outer and inner segments (OS and IS). Cell bodies of photoreceptors form the outer nuclear layer (ONL). The first layer of synapses is called outer plexiform layer (OPL). The inner nuclear layer (INL) consists of cell bodies of horizontal, bipolar, and amacrine cells. The second synaptic layer is the inner plexiform layer (IPL), which is located above the ganglion cell layer (GCL).

Photoreceptors are highly compartmentalized cells, consisting of the light sensing outer segment, an inner segment (containing the cellular machinery), a cell body (containing the nucleus), an axon (transmitting electrical signals), and a terminal (containing synapses) (Figure 3).

Vision begins in the photoreceptor outer segments. These are stacked membrane folds (Figure 4) at the tip of the photoreceptor cell. In mouse cones, the outer segments are 13 µm long and 1.2 µm wide (Carter-Dawson and LaVail, 1979). Light is sensed in the outer segment by opsin molecules and encoded into an electrical signal via a molecular phototransduction cascade. The light sensitive molecule opsin is a G-protein coupled receptor, which is integrated in the cone photoreceptor membrane. The absorption of a photon by an opsin molecule triggers a transduction cascade, which ultimately leads to a decrease in transmitter release in the photoreceptor terminal.

When there is no light, the membrane of the outer segment is conductive for cations, which leads to a constant depolarization of the photoreceptor cell. In this depolarized state, the neurotransmitter glutamate is continuously released at the terminal. In the presence of light, opsin molecules in the outer segment isomerize, cGMP concentration lowers, and cGMP-gated ion channels close. Consequently, the cation conductance is reduced, the cell hyperpolarizes, and transmitter release decreases.

The outer segment is a dynamic structure. Each day, an estimated 10-20% of each outer segment is renewed (Jonnal et al., 2010). The outer segment's upper part is phagocytosed by an adjacent tissue, the retinal prigment epithelium, while new membrane is produced and folded at the lower part of the outer segment (Mustafi et al., 2009).

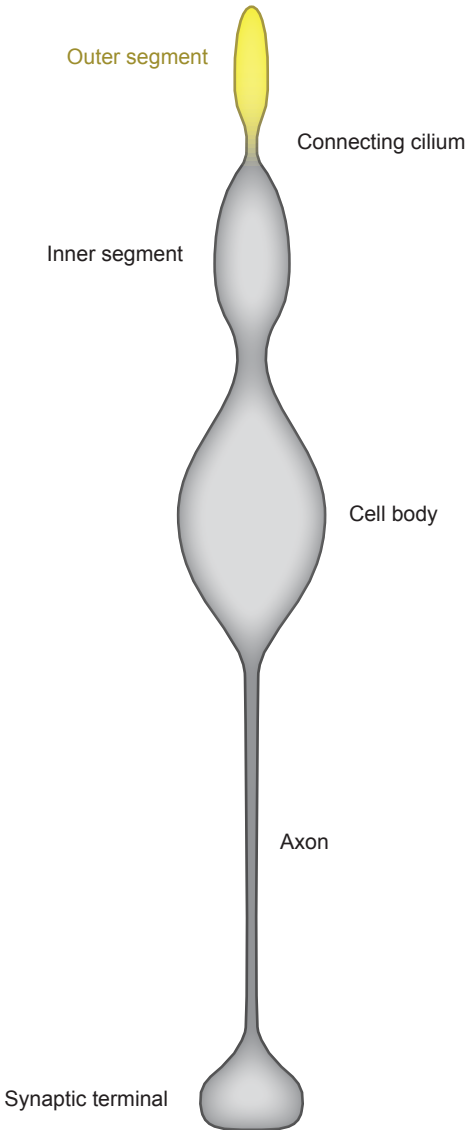

Figure 3. Cone photoreceptor. A cone photoreceptor consists of five compartments: the outer segment (yellow), in which light is detected; the inner segment, which contains the cellular machinery; the cell body, which contains the nucleus; the axon, which transports electrical signals; the terminal, in which ribbon synapses are made with bipolar and horizontal cells.

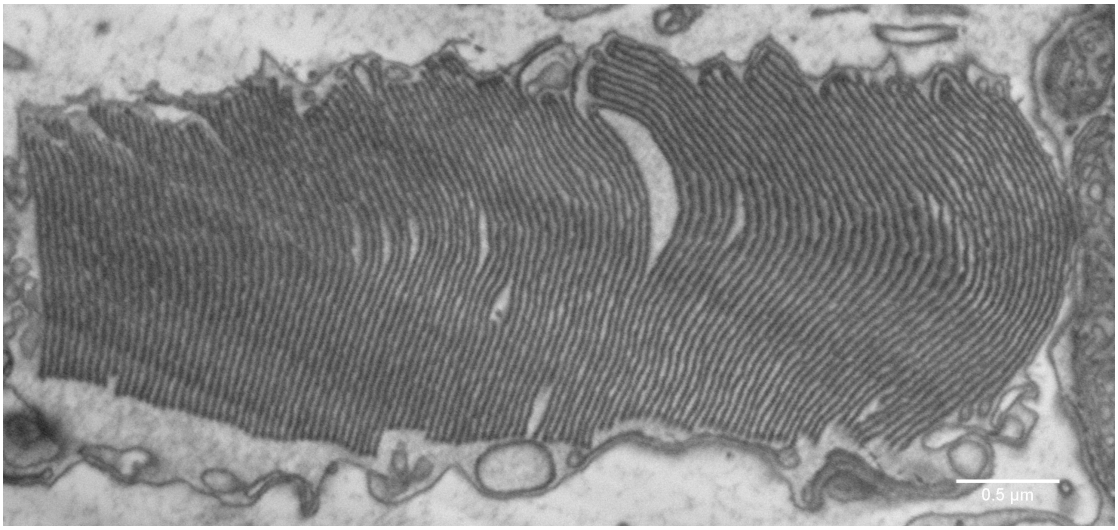

Figure 4. Membrane stacks of a cone photoreceptor. Scanning electron microscopy image of a cone photoreceptor outer segment of a lizard. Outer segments consist of stacked membranes, which house the proteins of the phototransduction machinery.

The consequence of a number of genetic diseases is the loss of the cone outer segment, which causes blindness (Sahel and Roska, 2013). Approximately half of all cases of blindness are due to the loss of the outer segment. Once outer segments are lost, cones slowly degenerate. However, there is a significant time window during which degenerating cones have lost their outer segments (and hence their ability to detect light), but the rest of the cell remains alive (Sahel and Roska, 2013). Therefore, there is a therapeutic time window during which outer segments could potentially be regenerated to restore light sensitivity.

There are two conceptually different ways of gaining insight into potential routes for outer segment regeneration: first, understanding how they are formed during embryonic/postnatal development, and second, understanding how they are maintained, i.e. how their renewal is regulated. During my PhD, I uncovered the mechanism that drives outer segment formation (Project 1, main project) and

I contributed to the understanding of how outer segment are maintained (Project 2, side project). In project 1, I was the single first author, and in project 2, I was the second co-author.

2 | Project 1 | Main project

Outer segment formation

The formation of the light-sensing compartment of cone photoreceptors coincides with a transcriptional switch

2.1 | Background

There are two phases of specification from a progenitor cell to a functional cone photoreceptor during development: an early phase that determines the cellular fate; and a later phase that determines the full functionality of a cone. Cone fate is established in newly postmitotic progeny that are born from mitotic progenitor cells during embryonic development. In the mouse, this is between embryonic day 10 (E10) and E18 (Wang and Cepko, 2016; Swaroop et al., 2010; Brzezinski and Reh, 2015). Thus, the genetic fate of cones is established before birth. However, the key functional compartment, the outer segment, only develops postnatally (Obata and Usukura, 1992; Duncan and Herald, 1974; Sedmak and Wolfrum, 2011; Olney, 1968), and the cone can respond to light by the second postnatal week (Gibson et al., 2013). As cones are not dividing anymore at that stage, any regulation guiding the functional maturation needs to be implemented independently of the

cell cycle. While much is known about the molecular program that establishes cone fate (Emerson et al., 2013; Swaroop et al., 2010), little is known about the molecular program that governs the formation of the cone outer segment.

To get an insight, we correlated the formation of outer segments, gene expression, and chromatin accessibility of mouse cones daily between birth and eye opening, using serial block-face electron microscopy, RNA sequencing, ATAC sequencing, and bioinformatic analyses. Our analysis concentrated on the central retina because the retina develops asynchronously, from the center to the periphery.

2.2 | Results

2.2.1 | Cone outer segments of the central retina appear rapidly at P6

We monitored the formation of outer segments in developing postmitotic photoreceptors in the central region of the mouse retina. We analyzed ten different time points from postnatal day 0 (P0) to P11 by 3D reconstructing the ultrastructure of the photoreceptor layer using serial block-face electron microscopy (Denk and Horstmann, 2004; Busskamp et al., 2014a). To ensure an intact ultrastructure of the outer segments we kept the photoreceptor layer together with the retinal pigment epithelium. We identified photoreceptor outer segments as subcellular structures with stacked electron-dense membranes at the tip of a connecting cilium. Outer segments were absent until P4, their number abruptly increased from 7% of the cells having an outer segment at P5 to 53% at P6, and then continued to increase until P11 (Figure 1, Figure 2, and Figure 6).

With electron microscopy it is possible to definitely identify outer segments

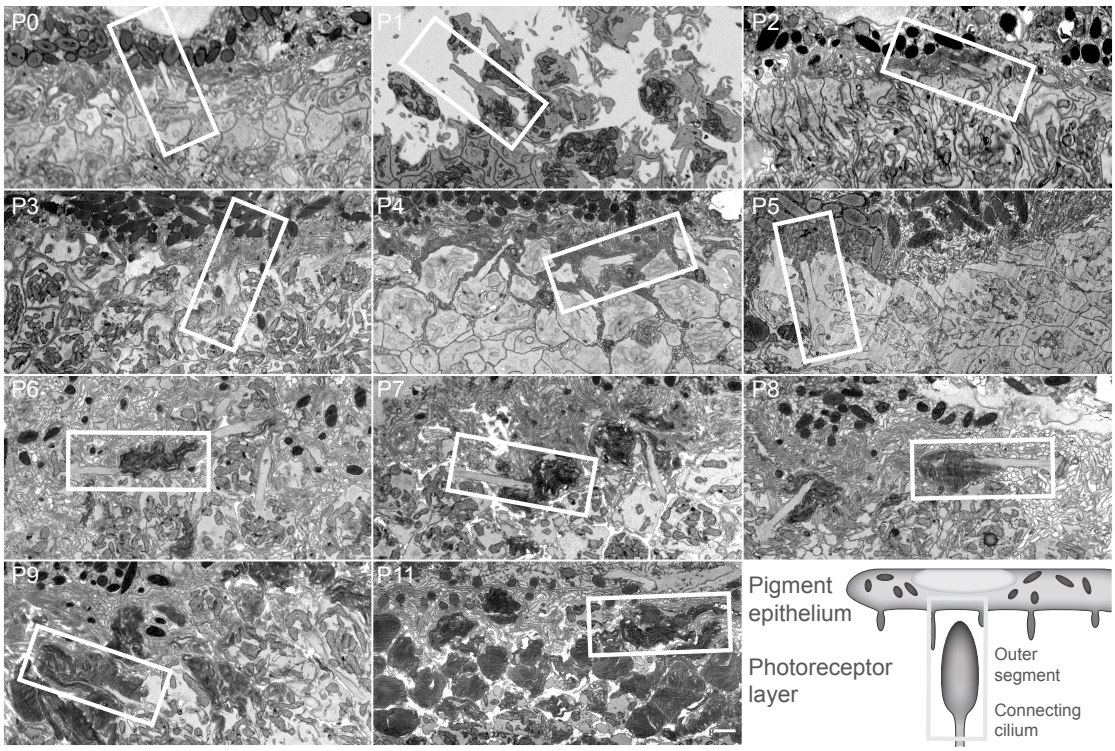

Figure 1. Ultrastructure of photoreceptors at different postnatal days. Each panel shows a single image from a serial block-face electron microscopy image stack at the indicated postnatal day. Pigment epithelium is attached at all time points except P1. The white boxes indicate regions that are shown in Figure 2. Scale bar 1 µm.

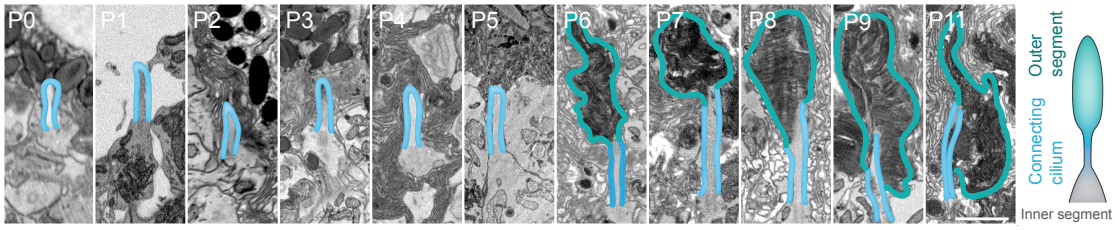

Figure 2. Ultrastructure of photoreceptor compartments at different postnatal days. Outer segments in cyan; connecting cilium in blue. Each panel shows a single image from an image stack obtained by serial block-face electron microscopy, magnified from a region marked in Figure 1. Scale bar 1 µm.

but it is not possible to differentiate between rods and cones at early postnatal stages. To follow the development of cone outer segments specifically, but at lower resolution, we used a mouse line (Chrnb4-GFP) that selectively expresses GFP in cones 16 and we monitored cone outer segment development using light microscopy.

First, we verified the specificity of GFP expression in cones (Siegert et al., 2009) from P0 to P12 by immunohistochemistry using a mixture of antibodies against short- and middle-wavelength cone opsins. Between P3 and P11, 98% of GFP-positive cells were found above the inner plexiform layer (IPL, in the adult retina all photoreceptors are found above the IPL). 94% of those GFP-labeled cells were positive for cone opsin, indicating that they are cones (Figure 3). Conversely, 99.1% of opsin positive cells were labeled with GFP, indicating that most cones are GFP-labeled (Figure 3). Therefore, from P3 onwards, cones were specifically and extensively labeled in the Chrnb4-GFP mouse line.

We then followed the distal tip of GFP-labeled cells every day from P0 to P12. Up to P4, opsin labeling was weak and it was confined to the cell body and inner segment, with no opsin-rich extension at the distal tip (Figure 4 and Figure 5). At P5, very few short opsin-labeled tip extensions appeared. We interpreted these extensions as outer segments. The number of opsin-rich extensions abruptly increased from 4% at P5 to 45% at P6, and then continued to increase until P12 (Figure 6).

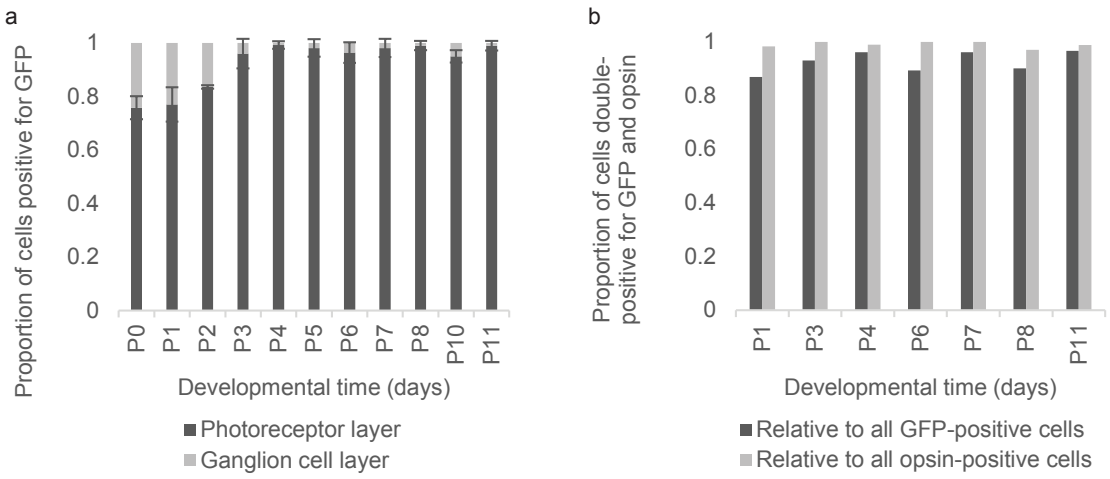

Figure 3. The identity of GFP-labeled cells in the retina of Chrnb4-GFP mice. (**a**) The distribution of GFP-positive cells across the different layers of the retina at different developmental days. The proportion of GFP-positive cells in the ganglion cell layer and in the photoreceptor cell layer relative to the total number of GFP-positive cells is shown. The quantification was performed on confocal microscopy images taken from retinal vibratome sections (n=3 mice per day). Error bars show means ± s.d. (**b**) The proportion of cells in the photoreceptor layer that are positive for both GFP and cone opsin, relative to the total number of GFP-positive cells (dark grey) and relative to the total number of cone opsin-positive cells (light grey) is shown at different postnatal days. The quantifications were based on confocal microscopy images of retinal whole mounts stained against GFP and a mix of s- and m-/l-opsin (n=1 mouse per day).

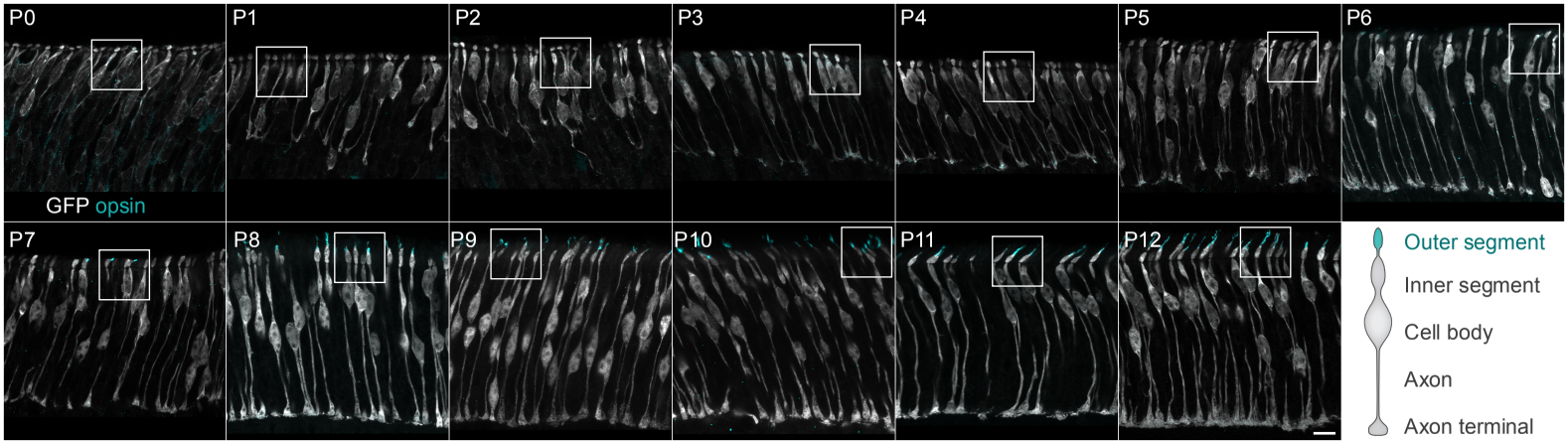

Figure 4. Opsin expression in cones of Chrnb4-GFP mice at different postnatal days. Each image shows a maximum intensity projection of a 7 µm stack of confocal microscopy images obtained from a retinal vibratome section. Cones stained with antibodies against GFP (grey) and a mix of antibodies against s- and m/l-opsin (cyan). Scale bar 10 µm.

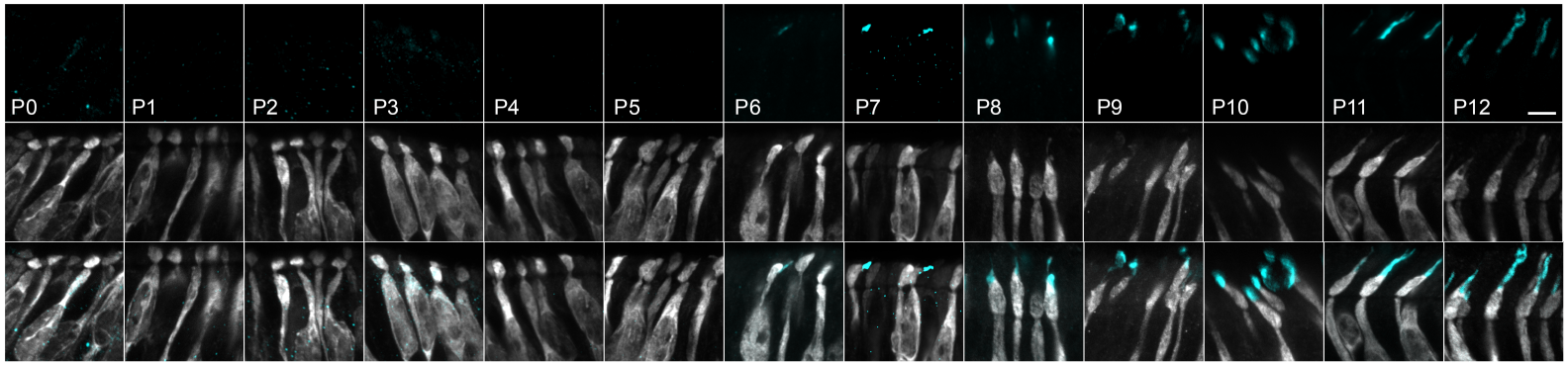

Figure 5. Opsin expression in inner and outer segments of cones of Chrnb4-GFP mice at different postnatal days. Magnification of regions marked in Figure 4. Upper row: opsin staining. Middle row: GFP staining. Lower row: GPF and opsin staining. Scale bar 5 µm.

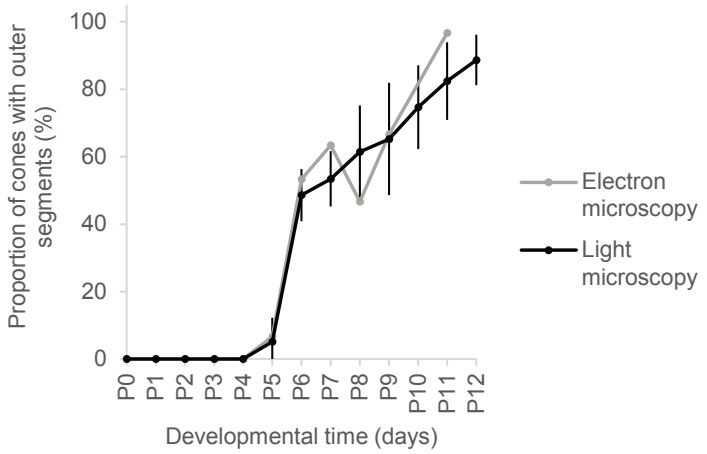

Figure 6. Quantification of outer segments. Quantification of data shown in Figure 1 and Figure 2 (n=1 mouse per day) and in Figure 4 and Figure 5 (n=3 mice per day). Error bars show means ± s.d.

Therefore, both the electron and light microscopic observations suggest that the fraction of cones that has outer segments rapidly increased from P5 to P6 in the central retina (Figure 6).

2.2.2 | Genome-wide gene expression switch at P6

To correlate the appearance of cone outer segments with the gene expression patterns of developing cones, we determined the transcriptomes of postmitotic cone photoreceptors in the central region of the mouse retina every day between birth (P0) and eye opening (P12). At each postnatal day we isolated GFP-labeled cells from three different Chrnb4-GFP mice (biological triplicates) using fluorescence-activated cell sorting. We then acquired the transcriptomes of the sorted cones using next generation RNA sequencing. Our data set contained 39 transcriptomes.

The transcriptomes of cones isolated before P6 correlated strongly with each

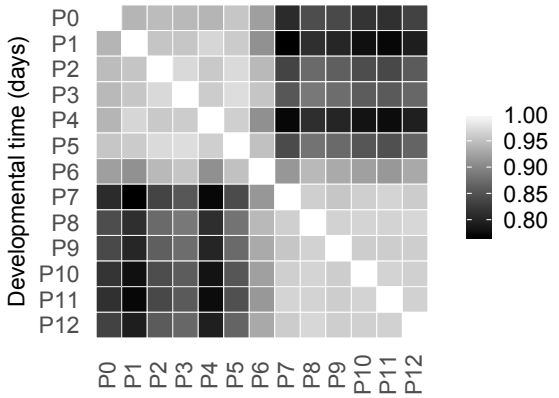

Figure 7. Correlation of RNAseq reads. Pearson correlations between the $\log_2$-transformed numbers of RNAseq reads per gene in cones isolated at different postnatal days from Chrnb4-GFP mice, three replicates per time point. R = Pearson correlation coefficient.

other (mean Pearson R = 0.96) (Figure 7). Likewise, correlation was high among transcriptomes of cones isolated after P6 (mean Pearson R = 0.97). However, the correlation between cones isolated before P6 and cones isolated after P6 was significantly lower (mean Pearson R = 0.8), suggesting a switch in gene expression around P6.

This switch could be one of many different temporal changes in gene expression between P0 and P12. Other types of temporal changes include the continuous rise of expression of some genes, and the continuous decrease of expression of others. To rank the different types of changes, we performed a principal component analysis (Methods). Each principal component describes a commonly occurring temporal change in gene expression, and its weight shows how much of the variance in the expression of all genes can be explained by this time course. The first principal component was characterized by a switch at P6: similar values from P0 to P5, a sudden change at P6, and then again similar values from P7 to P12 (Figure 8). This principal component accounted for 67% of the variance in gene expression,

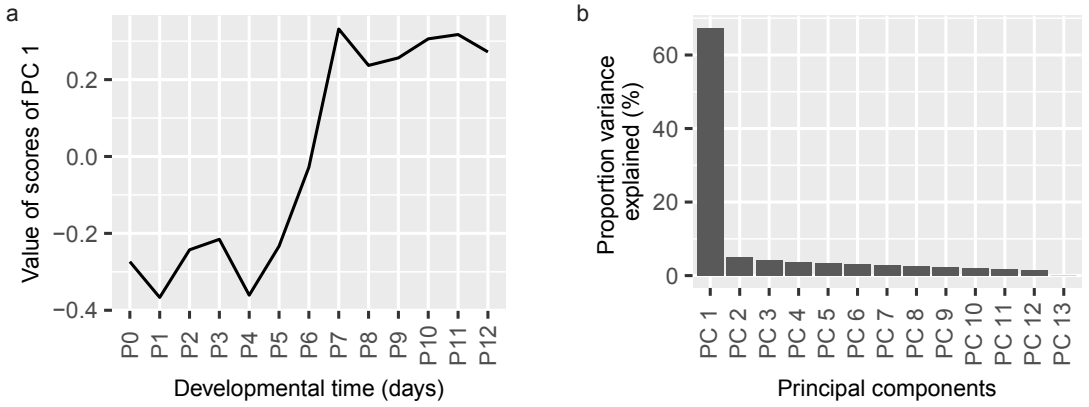

Figure 8. Principal component analysis. (**a**) The values of the first principal component, representing a common time course. (**b**) The proportion of variance explained by different principal components.

while the second principal component was responsible for only 5% of the variance (Figure 8). Therefore, a switch in gene expression at P6 is the dominant event in the time course of postnatal gene expression in the first two postnatal weeks.

A switch could mean a sudden decrease or an increase in gene expression. To understand the polarity of the change, we sorted the expressed genes according to the fold change of expression before and after P6. We found a group of genes that switched on (n = 508 "switch-on" genes) and another group of genes that switched off (n = 1038 "switch-off" genes) between 2- and 1,000-fold (Figure 9 and Figure 10). Therefore, 14% of all the 11,257 expressed genes switched expression at least 2-fold around P6 ("switch genes").

To determine whether the switch was a genome-wide phenomenon or whether particular chromosomes were more affected than others we analyzed the distribution of switch genes in the genome. We found that switch genes were distributed over the whole genome. The distribution of switch-on and switch-off genes was not different from the distribution of all genes (Chi square test, switch-on: p =

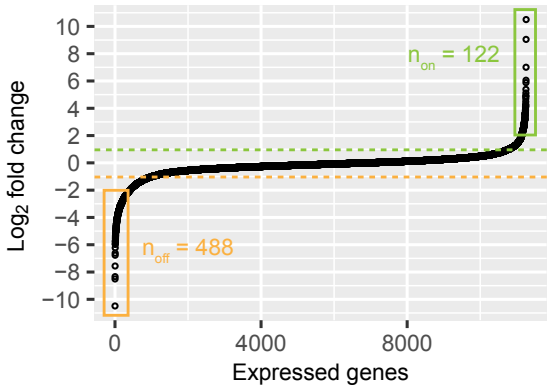

Figure 9. Changes in gene expression. Ordered $\log_2$ fold changes in expression of all 11,257 expressed genes in isolated cones. Fold changes are the difference in expression levels before (mean expression P0-P5) and after (mean expression P7-P12) the switch. Fold changes are ordered from smallest to largest value. Switch-on (non) and switch-off (noff) genes with absolute $\log_2$ fold changes higher than 2 (= $\log_2$ fold changes higher than 2 or lower than -2) are marked with a box. Switch-on and switch-off genes with absolute $\log_2$ fold changes higher than 1 are above or below the dashed lines.

0.279, switch-off: p = 0.5499) (Figure 11). We then analyzed the finer time course of switch-on and switch-off genes that switched at least 4-fold (n=122 "switch-on" genes and n=488 "switch-off" genes). We found that the switch started at P5 and ended at P7 (Figure 12). Thus, the switching genes are up- or downregulated at P6.

The switch in gene expression coincided with the sudden appearance of the outer segments: on the same day that the gene expression switch began, the growth of outer segments started (Figure 13).

2.2.3 | The identity of switch-on and switch-off genes

To better understand the gene expression switch, we analyzed which genes, gene classes, and pathways were involved. A large-scale transition in gene expression likely involves transcription factors. We therefore analyzed the frequency and

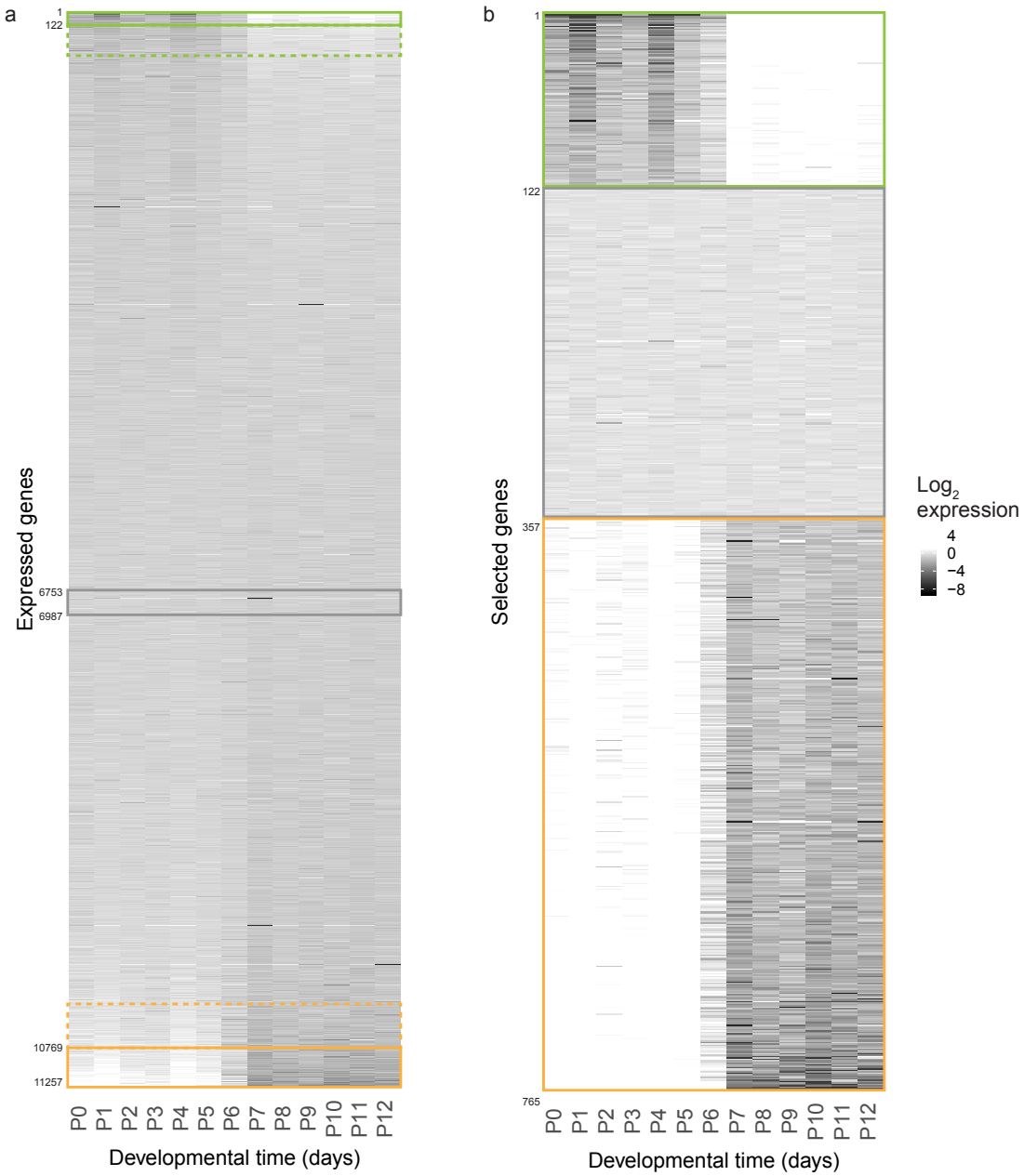

Figure 10. Gene expression levels. Heat maps showing expression levels for all expressed genes (**a**) and selected genes (**b**) from P0-P12. Rows show genes ranked by $\log_2$ fold change. Green and orange boxes correspond to regions marked in Figure 9. The grey box marks constant genes with absolute $\log_2$ fold changes less than 0.01. (**a**) Expression levels of all expressed genes. (**b**) Expression levels of switch-on and switch-off genes that have absolute $\log_2$ fold changes greater than 2, as well as constant genes.

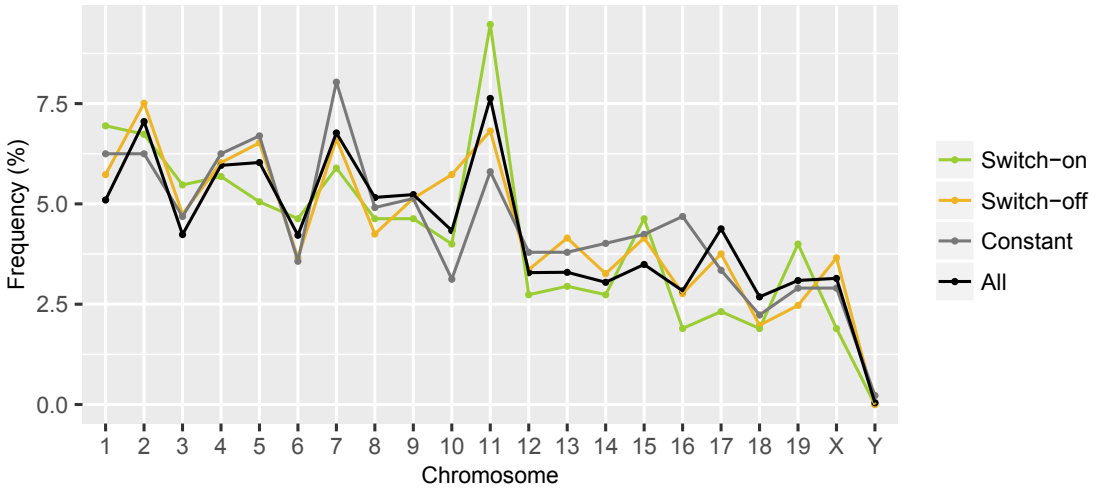

Figure 11. Switch genes are evenly distributed over the genome. Frequency of cone-expressed genes across different chromosomes in the mouse genome, shown for different groups of genes: all expressed genes (black); constantly expressed genes with absolute fold changes of $|\log_2$ fold change$| < 0.01$ (grey); and switch genes with $|\log_2$ fold change$| > 1$ (green and orange).

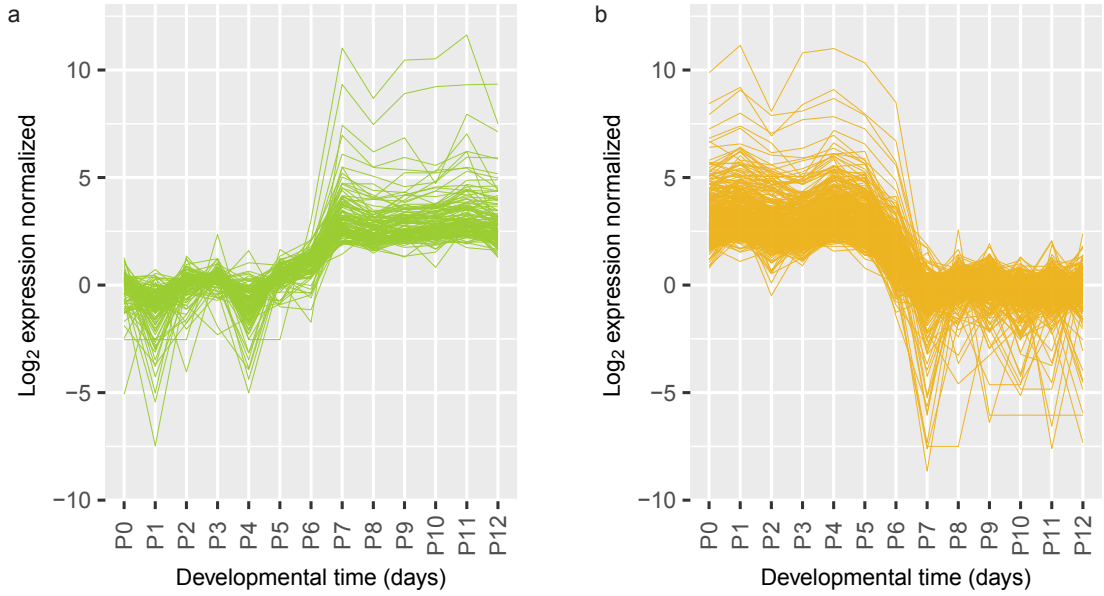

Figure 12. Time-course of gene expression changes. Time course of normalized $\log_2$ fold changes for switch-on genes (**a**) and switch-off genes (**b**) that have absolute $\log_2$ fold changes greater than 2. The data are normalized to the mean expression before the switch (P0-P5) (**a**) or after the switch (P7-P12) (**b**).

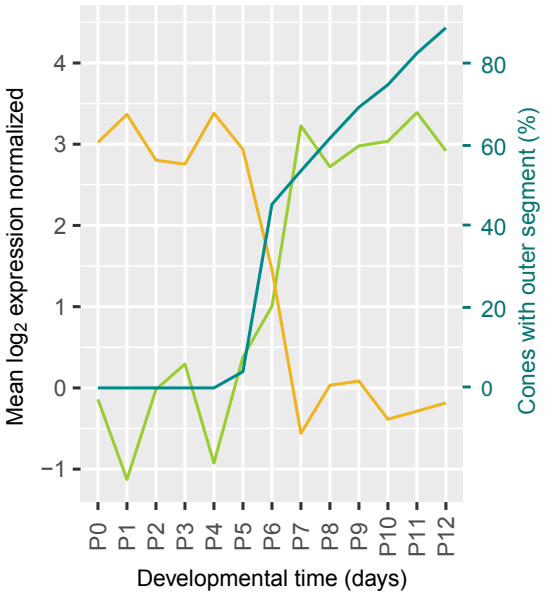

Figure 13. Correlation of gene expression changes and morphological changes. Mean $\log_2$ fold changes of switch-on and switch-off genes with absolute $\log_2$ fold changes greater than 2 and percentage of outer segments (replotted from Fig. 1d).

identity of transcription factors among switch genes. Among switch-off genes, we found four times more transcription factors than expected by chance: 23% of the top 100 switch-off genes were transcription factors, whereas the expected frequency of transcription factors in the entire transcriptome was 6% (Permutation test, $p = 9 \times 10^{-8}$) (Figure 14). In comparison, the frequency of transcription factors among the top 100 switch-on genes was not significantly different from the expected frequency (Permutation test, $p = 0.21$). The switch-off genes included five neurogenic transcription factors that are known to promote direct conversion of cultured fibroblasts or induced pluripotent stem cells to neurons (Vierbuchen et al., 2010; Busskamp et al., 2014b; Zhang et al., 2013; Pfisterer et al., 2011; Son et al., 2011). All five of these genes were strongly downregulated: Ascl1 188-fold, Myt1l 13-fold, Neurog1 74-fold, Neurog2 21-fold, and Pou3f2 (also known as Brn2)

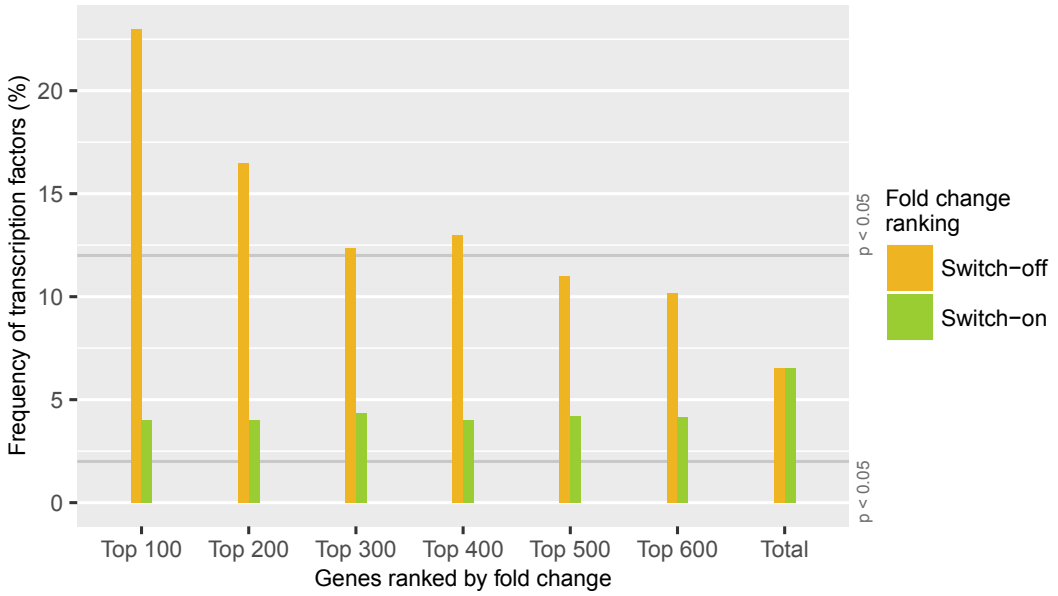

Figure 14. Switch-off genes contain a high proportion of transcription factors. Proportion of transcription factors among different groups of switch-on (green) and switch-off (orange) genes. All expressed genes were ordered by their $\log_2$ fold changes between P0-P5 and P7-P12 and the 100, 200, 300, 400, 500 and 600 most strongly on- or off-switching genes were grouped. The last group "total" contains all expressed genes (for conceptual consistency there are two separate bars but there is no difference between the orange and the green bar). The grey lines mark the frequency of transcription factors that is significantly higher or lower than expected (permutation analysis).

7-fold, resulting in expression levels below the detection threshold after the switch.

Many cone-specific proteins, including members of the phototransduction cascade, are located in the outer segment. As the growth of the outer segments and the regulation of switch genes began in parallel, we asked how cone-specific genes were distributed among switch genes. We defined 41 cone-specific genes based on a cell type transcriptome study (Siegert et al., 2012). The expression of this group of genes switched on significantly (Permutation test, $p < 10^{-6}$) (Figure 15 and Figure 16). Likewise, the phototransduction pathway switched on significantly (Permutation test, $p < 10^{-6}$) (Figure 15 and Figure 16). Therefore, cone-specific genes

and genes of the phototransduction pathway were among the switch-on genes.

Performing a global analysis for 219 other cellular pathways revealed that 50 pathways were significantly up- or downregulated in a switch-like manner (Permutation test, $p < 0.05$) (Figure 15). Among those 50 switch pathways, all of the metabolic pathways switched on, which shows a boost in energy metabolism at the time of outer segment formation (Figure 15 and Figure 16). On the other hand, pathways involved in Hedgehog signaling, Notch signal transduction, and axon guidance switched off (Permutation test, p=0.005, $p = 0.01$, and $p < 10^{-6}$, respectively) (Figure 15 and Figure 16).

Therefore, pathways essential for establishing a functional cone – with phototransduction and a high energy metabolism – switched on. In contrast, components of general neuronal development – such as neurogenic transcription factors and the axon guidance pathway – switched off.

2.2.4 | Regulation of the switching genes

A switch in gene expression can be regulated transcriptionally or post-transcriptionally. To differentiate between these two scenarios, we performed an exon-intron split analysis (Gaidatzis et al., 2015). We separately quantified RNA sequencing reads obtained from exons (from both pre-mRNA and mature mRNA) and reads obtained from introns (only from pre-mRNA), and we correlated the change of exonic and intronic reads before and after the switch. If a transcriptional mechanism is responsible for the switch, then the observed changes in exonic and intronic reads are expected to correlate. If, on the other hand, a post-transcriptional mechanism controls the switch, exonic and intronic reads are decoupled and a lower correlation is expected. The Pearson correlation between the changes in exonic and intronic

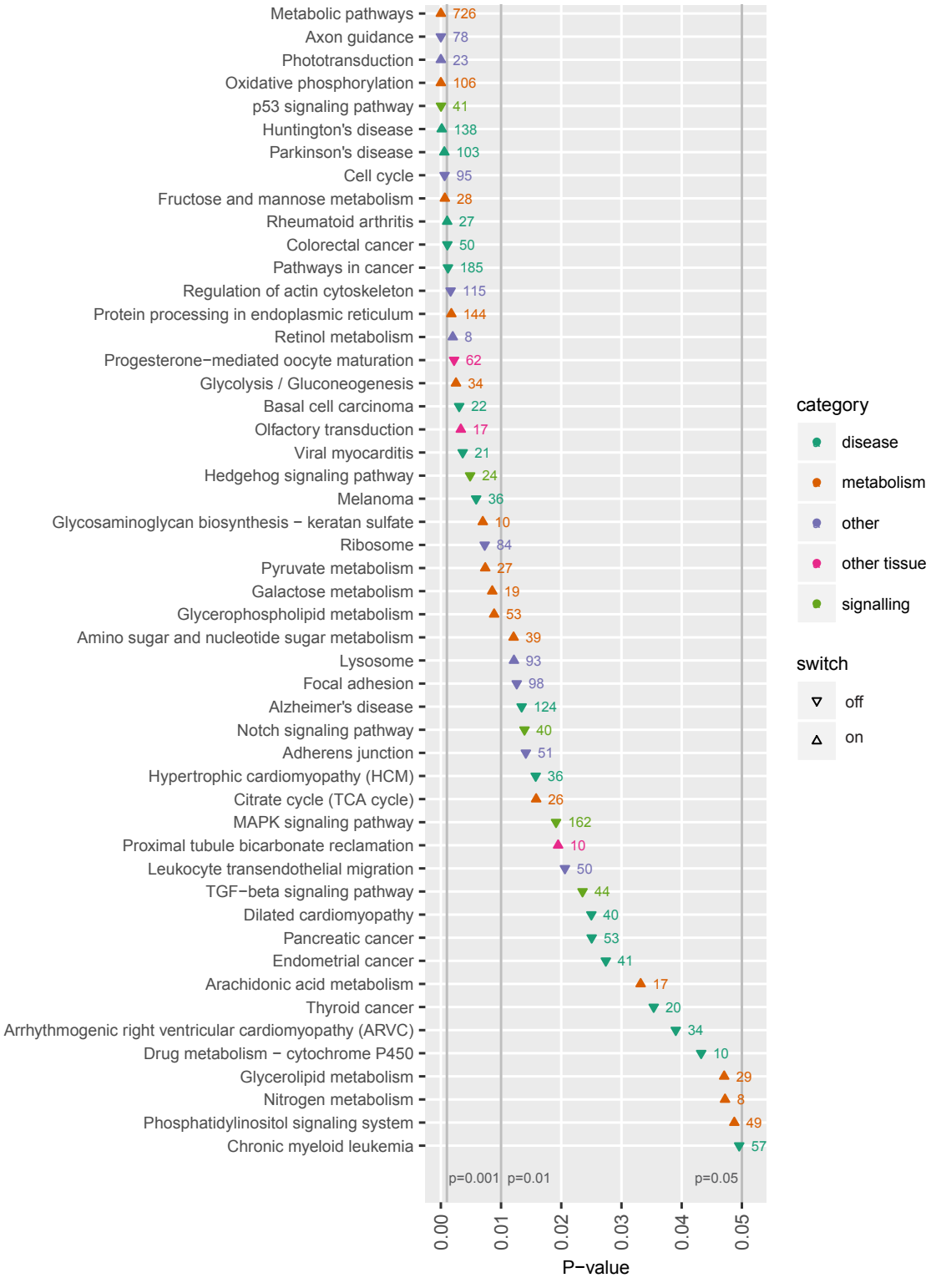

Figure 15. Pathways involved in the switch. All significantly up- or downregulated pathways are ordered by p-value (at 1 million iterations), and color-coded by category.

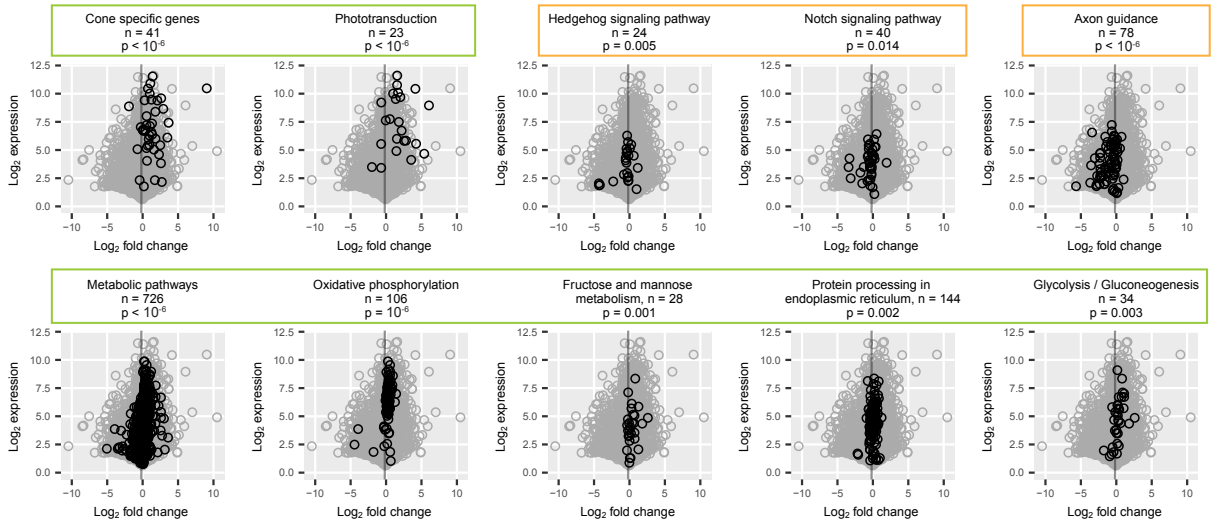

Figure 16. Expression changes of pathways involved in the switch. Comparison of $\log_2$ fold changes and $\log_2$ maximum expression levels during P0-P12 of all expressed genes (grey) with genes associated with a particular pathway (black): pathways needed for cone function, signaling pathways, axon guidance pathway, and metabolic pathways. The grey line marks the mean fold change of all expressed genes (-0.18). P-values from permutation analyses; n is the number of genes associated with each pathway. Orange boxes mark pathways that switch off, and green boxes mark pathways that switch on.

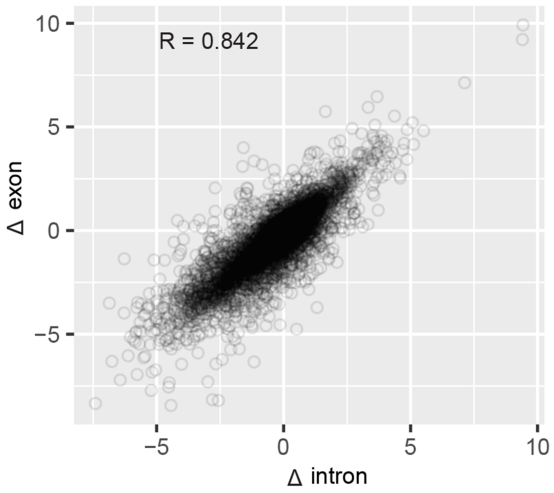

Figure 17. Transcriptional regulation of the switch. RNAseq reads quantified with an exon-intron split analysis 23 to differentiate transcriptional and post-transcriptional regulation of the switch. Correlation of $\log_2$ fold changes (Δ) in reads obtained from exons (from both pre-mRNA and mature mRNA) with reads obtained from introns (only from pre-mRNA). R = Pearson correlation coefficient.

reads was 0.84, suggesting that transcriptional changes accounted for at least 70% of the changes in gene expression during the switch (Figure 17).

As the switch was mostly regulated by a transcriptional mechanism, chromatin rearrangements could be involved in the regulation. To understand if chromatin architecture was rearranged, we mapped the accessible genome by ATACseq. This allowed us to determine which regions of the genome were free of nucleosomes and thus accessible to protein binding. We performed ATACseq at three time points: before the switch (P3), on the day of the switch (P6), and after the switch (P10). We obtained 70% mappable sequences (Figure 18), and identified 203,285 peaks of accessible DNA regions (regions of open chromatin). Regions of open chromatin correlated between P6 and P10, while the correlation between P3 and P6 was lower (Figure 19). We then counted regions that either lost or gained accessibility

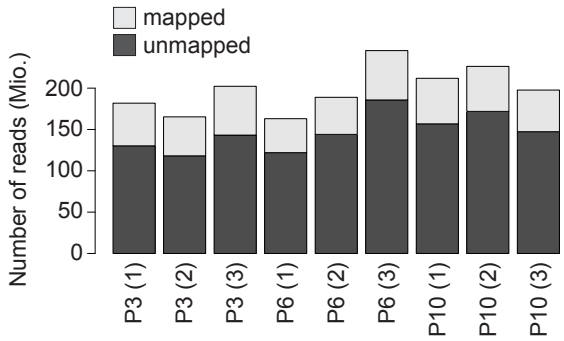

Figure 18. ATACseq mapping. Total number (in millions) of mapped and unmapped reads for each sample.

between P3-P6 and P6-P10, and we found a striking asymmetry (Figure 20). The vast majority of the changes happened prior to the transcriptional switch (between P3 and P6), when 26,014 regions lost accessibility and 5,687 regions gained accessibility. In contrast, only 172 regions lost and 114 gained accessibility after the switch (between P6 and P10).

We next compared chromatin accessibility of P3, P6, and P10 cones to adult cones and adult rods (Mo et al., 2016). As expected, all three samples correlated strongly with adult cones (R = 0.86), whereas, they correlated much less with adult rods (R = 0.32) (Figure 21). Furthermore, P6 and P10 cones correlated more with adult cones (R = 0.88) than P3 cones (R = 0.81).

The chromatin changes observed between P3 and P6 showed two characteristics. First, short regions changed more than large regions (Figure 23), and, second, distal regions changed more than proximal regions (Figure 22). Proximal regions are promoters, which lie within several hundred base pairs of the nearest transcription start site and are usually longer accessible regions. Distal regions are typically enhancers, which lie more than 1 kb away from the nearest transcription start site

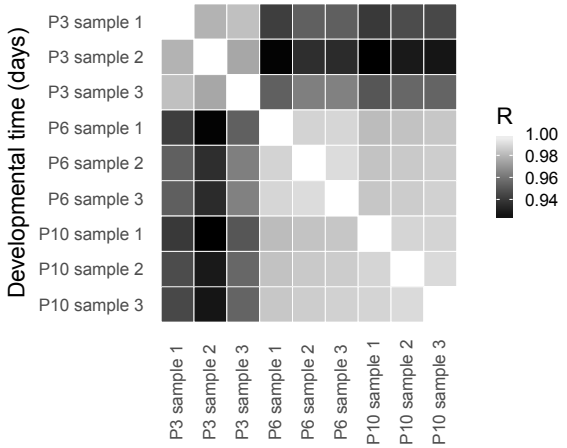

Figure 19. Correlation of ATACseq reads. Pearson correlations between the numbers of reads at each peak (a "peak" is a region of accessible chromatin) across different developmental days. R = Pearson correlation coefficient.

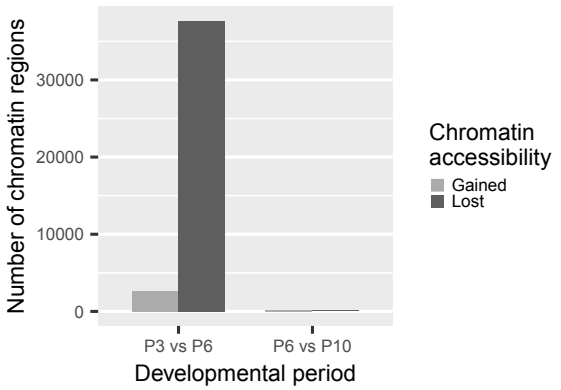

Figure 20. Chromatin accessibility changes. Changes of chromatin accessibility before (P3 vs. P6) and after (P6 vs. P10) the switch. The number of chromatin regions gaining (gray) or losing (dark grey) accessibility is shown. The threshold was an absolute $\log_2$ fold change of more than 1 and a false discovery rate less than 0.01.

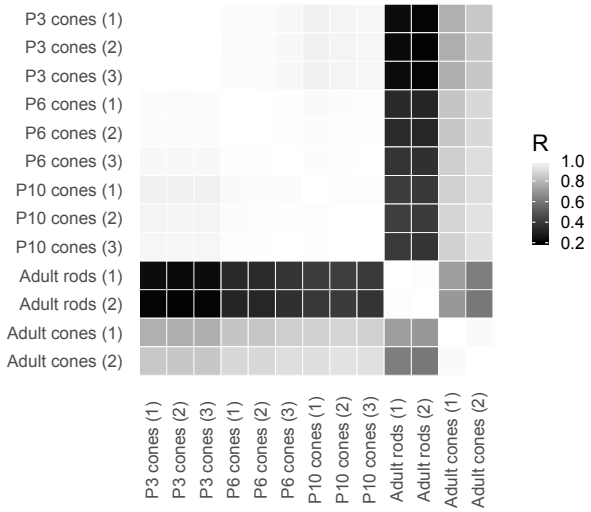

Figure 21. Correlation of ATACseq reads with reads from adult rods and cones. Pearson correlation between the $\log_2$-transformed numbers of reads at each region of accessible chromatin in developing cones compared to adult rods and cones. Data for adult rods and cones are taken from published ATACseq data (Mo et al., 2016), R = Pearson correlation coefficient.

and are generally short accessible regions. This suggests that there is a global chromatin accessibility loss that affected distal enhancers but not promoters.

A change in chromatin accessibility is often caused by an altered interaction between DNA binding proteins and specific regions on the DNA. To identify potentially relevant DNA binding proteins, we searched for distinct sequence motifs in differential peaks between P3 and P6. We used a regularized regression model (Friedman et al., 2010) to analyze how the presence of known DNA binding motifs contributed to the observed chromatin changes (Figure 24). Currently, only 23% of the transcription factors that are expressed in cones before or after the switch have annotated binding sites, which limits a full analysis. Nonetheless, we identified a single DNA binding protein, CTCF (Ong and Corces, 2014; Phillips and Corces, 2009), with an outstanding contribution to explaining the observed

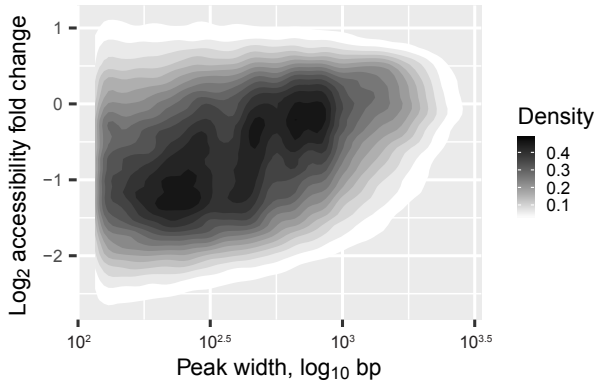

Figure 22. Short peaks change more than long peaks. Chromatin accessibility changes between P3 and P6 depending on the length of the region (in base pairs (bp), shown as the width of the peaks in Figure 27). The density of regions of accessible chromatin as a function of peak width and $\log_2$ fold change of accessibility is shown.

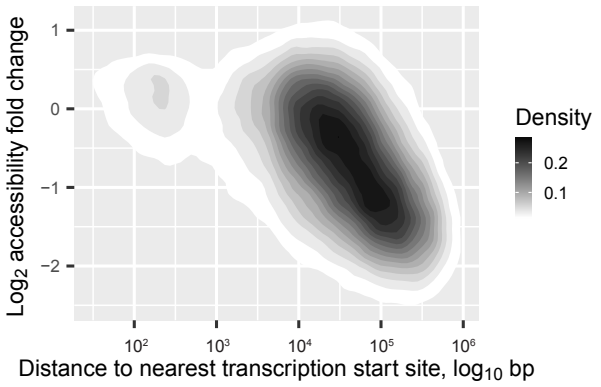

Figure 23. Distal peaks change more than proximal peaks. Changes of chromatin accessibility in identified peaks between P3 and P6 depending on the distance to the nearest transcription start site. The density of regions of accessible chromatin as a function of distance and $\log_2$ fold change of accessibility is shown. Density is indicated according to the gray scale on the right.

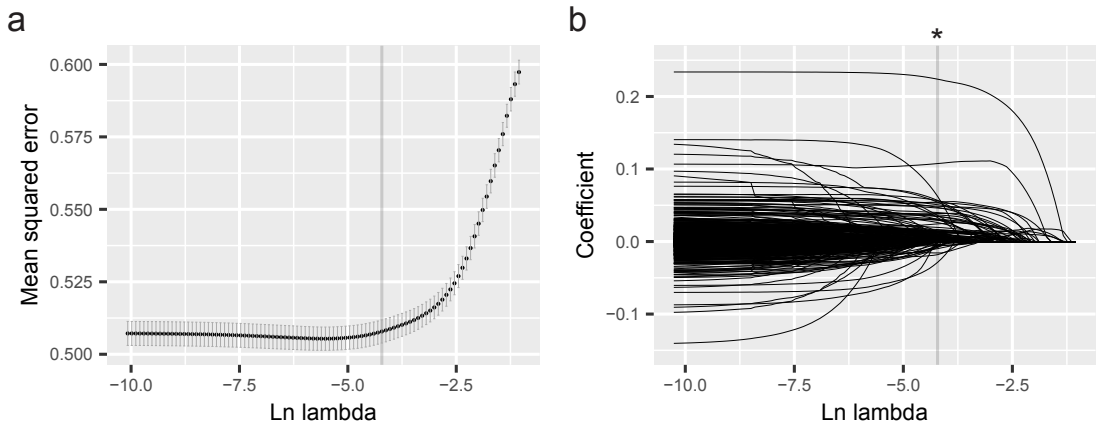

Figure 24. Prediction of DNA binding proteins. (**a**) Selection of lambda for the elastic net model by 5-fold cross-validation of lambda values (Methods). Mean cross-validated errors ± s.d. are shown. The grey line shows the highest lambda value at which the mean squared error was within one standard deviation of the minimal error. (**b**) Model coefficients for each predictor at different values of lambda. The grey line shows the chosen lambda value from (a). The asterisk marks the predictor with the highest coefficient (CTCF binding site).

accessibility changes (Figure 24). Are regions that can bind CTCF protected from chromatin accessibility changes before the transcriptional switch? We quantified the number of CTCF binding sites within each region of open chromatin, and found that the more CTCF binding sites a region contained, the more stable its chromatin accessibility remained (Figure 25). This suggests that regions without CTCF binding sites had a higher probability of losing accessibility between P3 and P6, than regions with CTCF binding sites.

Therefore, the switch was mostly regulated transcriptionally, and a genome-wide loss in chromatin accessibility preceded the switch. These chromatin changes predominantly affected enhancers, and in particular regions that lacked CTCF binding sites.

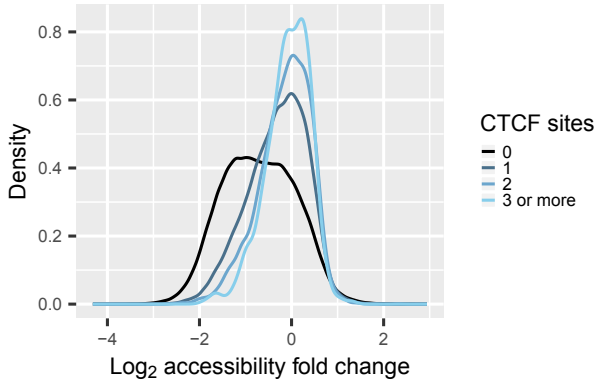

Figure 25. Regions without CTCF binding sites loose chromatin accessibility between P3 and P6. The number of binding sites for the protein CTCF was predicted for each region of accessible chromatin, and the regions of accessible chromatin were separated into four groups: regions without CTCF binding sites (black); regions containing 1 binding site (dark blue); regions containing 2 binding sites (blue); and regions containing 3 or more binding sites (light blue). The density of regions of accessible chromatin was plotted as a function of the $\log_2$ fold changes of chromatin accessibility, for each group separately.

2.3 | Discussion

By correlating the ultrastructure and gene expression of cones during postmitotic development, we found a major switch in cone morphology and gene expression at P6. The switch involves 14% of all expressed genes, and coincides with the formation of cone outer segments. Pathways essential for establishing a functional cone switch on, while components of general neuronal development switch off. The switch is mostly regulated transcriptionally, and is preceded by a genome-wide loss in chromatin accessibility. Enhancer elements – particularly regions without CTCF binding sites - were mostly affected by the chromatin accessibility loss. To our knowledge, no such fast and extensive change in gene expression and chromatin accessibility, correlated with a distinct morphological change, has been reported in neurons.

Our structural analyses indicate that the formation of cone outer segments starts between P5 and P6 in the central retina. Outer segment formation is rapid and synchronized, and by P6, 53% of the outer segments are already present in some form. It is known that the retina develops in an asynchronous fashion: the central part of the retina being at an advanced developmental stage compared to the periphery (Holt et al., 1988). This wave of maturation explains why previous studies analyzing the whole retina found a more gradual change compared to what we found analyzing only the central retina (Obata and Usukura, 1992; Duncan and Herald, 1974; Sedmak and Wolfrum, 2011; Olney, 1968).

Do rod outer segments also appear rapidly at P6? Our electron microscopy reconstructions of the photoreceptor layer contained both cone and rod photoreceptors. Morphologically, cones and rods are indistinguishable during early postnatal development. Since rods outnumber cones in the mouse retina, rod outer segments must also be present in our analysis and, therefore, also appear rapidly at P6. In this work, we chose to investigate cones, for two reasons. First, because they are highly important for human daylight vision. Second, because the determination of the cone cell fate occurs prenatally, which is shifted in time from outer segment formation. This shift allows the clear separation of the changes in gene expression associated with the two processes. Based on the structural and functional similarities between rods and cones, and based on a recent study, which showed large-scale gene expression changes between P6 and P10 in rod photoreceptors (Kim et al., 2016), it is possible that rods also show a gene expression switch between P5 and P7. Further studies at a fine temporal resolution are needed to investigate this possibility.

The analysis of gene classes and pathways that are involved in the switch has

revealed insights into the function of the switch. First, switch-off genes contain a high proportion of transcription factors, including Ascl1, Myt1l, Pou3f2 (also known as Brn2), Neurog1, and Neurog2. These neurogenic transcription factors are known to be - in different combinations - necessary and sufficient to promote direct conversion of cultured fibroblasts or induced pluripotent stem cells to neurons (Vierbuchen et al., 2010; Busskamp et al., 2014b; Zhang et al., 2013; Pfisterer et al., 2011; Son et al., 2011). In neurons, these factors continue being expressed throughout the lifetime of the cell (Allen Brain Atlas, 2016). This suggests that the neuronal state is turned off before cones become functional sensory cells. Second, switch-on genes include pathways needed for light detection (Siegert et al., 2012), as well as pathways for energy supply necessary for light detection. The late switch-on of metabolic pathways may save energy until it is needed for maintaining light responses.

The mechanism of the switch involves epigenetic changes. We found that the switch is mostly controlled transcriptionally, which we determined using an exon-intron split analysis. This is consistent with our finding that the switch was preceded by a large-scale loss of chromatin accessibility. This loss of chromatin accessibility only affected regions distal to the transcriptional start site, suggesting that the switch decreases accessibility at enhancer elements. Interestingly, the chromatin changes preferentially targeted regions that lacked CTCF binding sites. CTCF participates in the global organization of chromatin architecture by regulating the interplay between higher-order chromatin structure and cell-type-specific gene expression during development (Ong and Corces, 2014; Phillips and Corces, 2009). These findings indicate that a global chromatin rearrangement occurs during the switch.

What triggers the switch in gene expression at P6? Either a precisely timed regulatory event from outside the retina, or an internal clock within the retina. An internal clock would be the accumulation of a signal that triggers the switch once it reaches a threshold. This clock could reside either in cones or in other retinal cells. Opn1mw (encoding middle-wavelength opsin) is one of the genes that is not expressed in cones before P6 and whose expression switched on at P6. Opn1mw expression also turns on in vitro in cultured retinal explants (Satoh et al., 2009; Wikler et al., 1996), if the retina is cultured from P3 onwards. If the other switch genes behave similarly to Opn1mw in vitro, the switch is either triggered by an intra-retinal clock or by an extra-retinal signal that acts before P3 and has a delayed effect. Intriguingly, there is another switch-like event at P6 in another type of postmitotic retinal neuron, the retinal ganglion cells. In retinal ganglion cells, the neurotransmitter GABA is excitatory before P6 and inhibitory after P6. This excitatory-to-inhibitory switch is caused by a sudden change in chloride concentration within ganglion cells (Zhang et al., 2006). For both the excitatory-to-inhibitory switch in ganglion cells (Barkis et al., 2010) and the gene expression switch in cones that we report here, the trigger is not known. Elucidating the trigger for the gene expression switch in cones could help to establish a causal relationship between the switch and the formation of outer segments, and may help to find strategies to regenerate the outer segments of cones in blinding diseases.

2.4 | Methods

2.4.1 | Animals

Tg(Chrnb4-EGFP) mice were purchased from MMRRC. Animal procedures were done in accordance with standard ethical guidelines (European Communities Guidelines on the Care and Use of Laboratory Animals, 86/609/EEC) and were approved by the Veterinary Department of the Canton of Basel-Stadt. Mice were housed with a 12 hours dark-light cycle.

2.4.2 | Immunohistochemistry

After eyes were enucleated, they were either fixed as a whole eye for 3 h or retinas were dissected and only the retinas were fixed for 30 min. The fixative was 4% paraformaldehyde (Sigma-Aldrich) in phosphate-buffered saline (PBS). If the whole eye was fixed, eyecups were dissected after fixation by removing the anterior chamber of the eye in PBS. Eyecups and retinas were washed in PBS three times for a minimum of 30 min at room temperature (RT). The samples were dehydrated in 30% sucrose for minimum 30 min at RT and then treated with three freeze-thaw cycles. All eyecups and some of the retinas were embedded in 3% agarose (SeaKem Le Agarose) in PBS, and 150 µm sections were cut using a Leica VT1000S vibratome. The remaining retinas were processed without sectioning. Sections and whole-mount retinas were incubated in blocking solution for 1 h at RT. The blocking solution contained 10% normal donkey serum (Chemicon), 1% bovine serum albumin, and 0.5% Triton X-100 in PBS, at pH 7.4. Antibodies were diluted in 3% normal donkey serum, 1% bovine serum albumin, 0.02% sodium acid, and 0.5% Triton X-100 in PBS. Primary antibodies were applied for at least

1 day. The following antibodies were used: chicken-anti-GFP (1:500, Chemicon, AB16901), rat-anti-GFP (1:500, Nacalai/Brunschwig, 04404-84), goat-anti-S-opsin (1:200, Santa Cruz, sc-14365), goat-anti-M/L-opsin (1:200, Santa Cruz, sc-22117), rabbit-anti-S-opsin (1:200, Millipore, AB5407), and rabbit-anti-M/L-opsin (1:200, Millipore, AB5405). Retinas were then washed three times for 10/30 min (sections/whole mounts) in PBS, and incubated in the following secondary antibodies, all diluted at 1:200: Alexa Fluor 488 Donkey Anti-Chicken (Jackson Immuno, 703-545-155), Alexa Fluor 488 Donkey Anti-Rat (Life Technologies, a21208), Alexa Fluor 555 Donkey Anti-Rabbit (Thermo Fisher, A31572), Alexa Fluor 568 Donkey Anti-Goat (Thermo Fisher, A11057), Alexa Fluor 647 Donkey Anti-Rabbit (Life Technologies, A31573), and Alexa Fluor 647 Donkey Anti-Goat (Thermo Fisher, A21082). Nuclei were stained with 10 µg/ml of Hochst (Thermo Fisher, 62249) at a dilution of 1:500. Secondary antibodies and Hochst were applied for 1 h at RT, followed by three washes in PBS of 10/30 min each (sections/whole mounts), both in the dark. Sections and whole mounts were mounted on slides with ProLong Gold antifade reagent (Thermo Fisher, P36934).

2.4.3 | Light microscopy

Confocal three-dimensional scans were taken with a Zeiss LSM 700 Axio Imager Z2 laser-scanning confocal microscope using Plan-Apochromat 63×/1.40 Oil DIC M27 or EC Plan-Neofluar 40×/1.30 Oil M27 oil-immersion objective lenses at four excitation laser lines (405 nm for Hochst, 488 nm for GFP, and 555 nm or 639 nm for opsin). Optical sections of 1 µm were acquired.

2.4.4 | Light microscopy image analysis

Zeiss three-dimensional scan files (lsm format) were opened in Fiji ImageJ and processed as follows for quantification. First, optical sections were projected using a maximum intensity projection. For the compartmentalization analysis in vibratome sections, seven optical sections were projected. For the control experiments in vibratome sections, five optical sections were projected. For the control experiments in whole mounts, a single plane at the level of the inner and outer segment was analyzed. If necessary, the minimum or maximum pixel values were narrowed. Brightness or contrast were never changed. Cells were counted manually using the Cell Counter plugin. For the compartmentalization analysis, all cells (22 cells on average) were counted in each image (n=9 (3 animals, 3 regions each)), and the presence/absence of an outer segment was quantified. The example images in Fig. 1 are identical to the quantified images. For the control experiments in vibratome sections, all GFP-positive cells across all layers of the retina (39 cells on average) were counted in each image (n=3 (3 animals, 1 region each)), and the presence of GFP-positive cells outside the photoreceptor layer was quantified. For the control experiments in whole mounts, all cells were counted (112 cells on average) in each image (n=1), and it was quantified how many cells were positive for GFP and opsin (labeled cones), and how many were only positive for GFP (labeled rods) or only positive for opsin (unlabeled cones).

2.4.5 | Electron microscopy sample preparation

Eyes were enucleated and a small hole was made in the eye using a 27 G needle to allow influx of fixative. From the hole, the cornea was cut three times with

small scissors towards the sclera, approximately 2 mm per cut, to further open the eye. Eyes were placed in fixative containing 2% paraformaldehyde (EMS 15700), 1% glutaraldehyde (EMS 16300), and 2 mM CaCl2 (Sigma Aldrich 53704) in 0.3 M cacodylate (Sigma Aldrich 20838) at pH 7.4. Eyes were fixed overnight at 4 °C. The next day, retinas were dissected in 0.15 M cacodylate. Retinas were then vibratome sectioned as described above. The sections were stained using a standard protocol (https://www.ncmir.ucsd.edu/sbem-protocol/) with small modifications. Retinal sections were washed five times 3 min in 0.15 M cacodylate. Next, they were postfixed in a reduced osmium solution for 1 h on ice. The solution contained 3% $K_4Fe(CN)_6$ (Sigma Aldrich, 31254), 0.3 M cacodylate buffer, and 4% aqueous OsO_4 (EMS, 1/9100). Then, the samples were washed five times 3 min in ddH_2O and incubated in TCH solution for 20 min at RT. The TCH solution was made freshly each time, by incubating 1% thiocarbohydrazide (Sigma Aldrich, 88535) in ddH_2O for 1 h at 60 °C. It was swirled three times during the incubation and cooled down to RT after. Before usage, it was filtered using a 0.22 µm syringe filter (VWR, 514-0072). The second postfixation was done using 2% OsO_4 in ddH_2O for 30 min at RT. This was followed by five times 3 min wash in ddH_2O. The samples were then incubated in 1% uranyl acetate in ddH_2O overnight, and afterwards washed five times 3 min in ddH_2O. Next, they were incubated in Walton's lead aspartate for 20 min at 60 °C. Walton's lead aspartate was prepared by adding 0.66% lead nitrate (EMS, 17900) to 60 °C warm 0.03 M aspartic acid (Sigma Aldrich, 1043819), and the mix was incubated at 60 °C for 30 min. The pH was adjusted to 5.5 with 1 M NaOH (Sigma Aldrich, 72068) at 60 °C. After Walton's lead aspartate treatment, retinal sections were washed five times 3 min in ddH_2O at RT, and afterwards dehydrated with ethanol, each concentration

for 2 min: 50%, 70%, 90%, 95%, 100%, and 100% plus an additional 2 min in cold propylene oxide. Then the samples were incubated in 50% propylene oxide and 50% resin for 2 h. For the resin, 20 ml Embed 812 (Serva, 21045), 6.25 ml 2-dodecenylsuccinic acid anhydride (Serva, 20755), 5 ml methyl nadic anhydride (Serva, 29452), and 0.325 ml N-benzyldimethylamine (Serva, 14835) were mixed. After that, samples were immersed in 100% resin for 1 h. Then, the sample was incubated in fresh resin overnight. Depending on the microscope used for imaging, samples were either embedded in fresh resin or in silver resin and dried at 60 °C for 48 h. Silver resin (Epo-Tek, EE129-4) was a mix of 1.25 g component A and 1 g component B. The embedded tissue blocks were trimmed to a size of 1000 × 300 × 1000 µm using a razor blade and glued on aluminum stubs for SBEM (Gatan) using cyanoacrylate glue.

2.4.6 | Electron microscopy

Retinas were imaged using scanning electron microscopes (Quanta, FEI and Merlin, Zeiss). Inside each microscope was an ultramicrotome (3View, Gatan), which can remove thin tissue sections and enable the acquisition of serial images of the block face of the tissue. Backscattered electrons were detected and the 3View DigitalMicrograph software was used to acquire the images. Images were acquired at pixel sizes of 2.1 to 16.7 nm and a section thicknesses of 50 to 100 nm.

2.4.7 | Electron microscopy image analysis

The serial images in dm3 format were imported into Fiji ImageJ. They were aligned using the automated alignment tool (multilayer mosaic) in TrackEM (Cardona et al., 2012), allowing only for translational movements. Compartments were

counted manually in TrackEM. In each image stack, 30 cells were analyzed for the presence or absence of an outer segment. Outer segments were identified as stacked electron-dense membranes at the tip of a connecting cilium.

2.4.8 | RNA sequencing

A protocol from Siegert et al. (Siegert et al., 2012) was used to dissociate retinal cells. Retinas were dissected in HBSS and incubated in an activated papain solution for 5 min at 37 °C. After removing the papain solution, retinas were washed with HBSS containing 2% FCS and then dissociated in HBSS containing 2% by triturating the tissue with a fire-polished Pasteur pipette. The suspension was filtered before FACS sorting. Per time point (P0 till P12), we FACS-sorted three retinas, each from a different animal. If 20,000 cells could not be obtained from one retina, retinas of different animals were pooled. Cells where sorted using a BD Influx cell sorter (Becton, Dickinson and Company, BD Biosciences, San Jose, CA USA) with the BD FACS Sortware sorter software (Version 1.01.654). The sort was performed with a 100 µm nozzle tip, at a sheath pressure of 19.0 psi, and a frequency of 28.90 kHz. The following gates were set: gate 1 was forward scatter FSC-Area against side scatter SSC-Area, gate 2 was FSC-Width against FSC-Height, gate 3 was SSC-Width against SSC-Height, and gate 4 was 530/40 (488 nm) against 710/50 (561 nm). RNA isolation was done using the Pico Pure kit. Total RNA amplification was done using the NuGEn Ovation RNA-Seq System V2 followed by library preparation with the Illumian TruSeq Nano DNA Sample prep protocol. Samples were sequenced in the Hiseq in 50 cycles, producing single-end reads.

2.4.9 | RNA sequencing analysis

Analysis was performed using the statistical software R using the QuasR package (Gaidatzis et al., 2015). Sequences were mapped to a reference mouse genome (GRCm38/mm10) using splicedAlignment=TRUE, which internally uses SpliceMap (Au et al., 2010) counted per gene (using known gene annotation from UCSC) and normalized to the gene length and library size (RPKM = reads per kilobase transcript and million reads in library). Outliers were excluded from the analysis by removing the highest of the 39 values for each gene. The mean of the technical triplicates was calculated and a threshold was set to remove noise. To find the optimal threshold, different thresholds were applied and a curve was fitted to the resulting data set. The skewness of the curve was used as a measure of normal distribution. The threshold that resulted in the skewness closest to zero was chosen (threshold 1.645 RPKM). For the analyses, RPKM values were $\log_2$ transformed. To avoid minus infinity values after the log transformation, a small pseudocount was added to all values that equaled zero (in 91 instances). The smallest number that was not zero was chosen and a random integer between 1 and 10 divided by 106 was added. For the principal components analysis (PCA) the data were centered (mean subtracted) and the genes were considered as variables. Fold change was calculated as the mean $\log_2$ expression after the switch (P7 to P12) minus the mean $\log_2$ expression before the switch (P0 to P5). Switch-on genes were defined as having a $\log_2$ fold change of 1 or more, switch-off genes were defined as having a $\log_2$ fold change of -1 or less. Constant genes were defined as having $\log_2$ fold changes between 0.01 and -0.01. The information on the chromosomal location of each gene was retrieved from Ensembl Biomart (`http://www.ensembl.org/biomart/`) for

the mouse genome GRCm38.p4. Cone-specific genes were defined chosen from a cell type transcriptome study (Siegert et al., 2012). The cellular pathways were obtained from the KEGG database (http://www.genome.jp/kegg/pathway.html). To analyze the frequency of transcription factors among up- and downregulated genes, all expressed genes were ordered according to their fold changes, both ascending (for downregulated genes) and descending (for upregulated genes), and binned to bins of 100, 200, 300, 400, 500, and 600 genes. The observed frequency in each bin was compared to the expected frequency by a permutation analysis. Sets of 100 genes were drawn randomly (1 million repetitions, with replacement) from all expressed genes, and the mean frequency of transcription factors among them was calculated. If the observed frequency occurred in less than 5% of the draws, a bin was considered to be significantly enriched for transcription factors. Analogously, cone-specific genes and pathways were tested for being significantly up- or downregulated. For the analysis, cone-specific genes were treated as a pathway. The mean fold change was calculated for each pathway and compared to the mean fold change of sets of randomly drawn fold changes. The number of elements in each set was the same as in the analyzed pathway. To determine the number of draws needed, p-values were compared at 10^2, 10^3, 10^4, 10^5, and 10^6 draws (Figure 26). They were found to be stable after 10^5 draws, and 10^6 draws were chosen for the analysis. The number of drawn fold changes equaled the number of genes in a given pathway. A pathway was considered to be significantly up- or downregulated if 5% or fewer of the means of the randomly drawn fold changes were equal to or smaller than the absolute value of the observed fold change. If the observed fold change was not observed in any of the 10^6 draws, the p-value was indicated as $p < 10^{-6}$. The exon-intron split analysis was performed as described

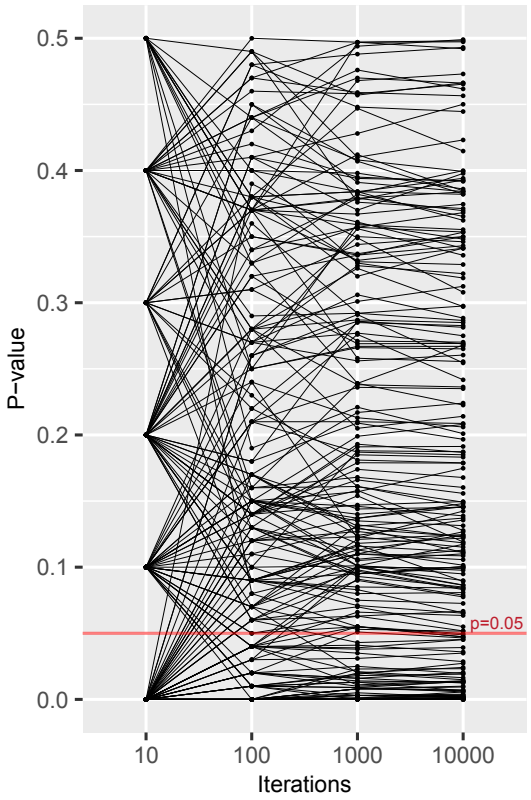

Figure 26. Selection of numbers of iterations for random draws. Changes in p-value as the number of random draws (iterations) in the permutation analyses increases. Each dot represents one pathway.

in Gaidatzis et al. (Gaidatzis et al., 2015). RNA sequencing reads obtained from exons and introns were quantified separately, and the change of exonic and intronic reads before and after the switch was correlated. The change was the difference between mean expression after the switch (P7 to P12) and mean expression before the switch (P0 to P5) in $\log_2$ space.

2.4.10 | ATACseq

Both retinas from mice age P3, P6, and P9 were used for the ATACseq experiment. For each time point, three mice were used. Only male mice were used to

avoid any influence from X-chromosome inactivation. The same procedure as for RNA sequencing was used for cell dissociation and FACS. Single-cell suspensions were obtained after FACS sorting into PBS/10%FCS. ATACseq was performed according to Buenrostro et al. (Buenrostro et al., 2013), with minor modifications. Briefly, 50,000 cells were used per transposition reaction. Cells were collected and lysed in cold lysis buffer (10mM Tris-HCl pH 8.0; 10mM NaCl; 3mM $MgCl_2$; 0.5% NP40). Transposition was done as reported in Buenrostro et al. (Buenrostro et al., 2013), steps 6 – 12, and PCR amplification was done according to steps 13 – 18. Briefly, during the amplification reaction, PCR primers were used as mentioned in the supplemental material from Buenrostro et al. (Buenrostro et al., 2013). Amplified libraries were cleaned up using AMPure XP beads in a DNA:beads ratio of 1:1.8. Further size selection of the library prior to sequencing was avoided. The Nextera DNA Library Preparation Kit was used for library preparation. Multiple experiments were sequenced per lane (up to 3 per lane). Libraries were sequenced paired-end 100 bp reads using the Illumina HiSeq.

2.4.11 | ATACseq analysis

Preprocessing of reads and analysis was performed using the statistical software R using the QuasR package (Gaidatzis et al., 2015). Briefly, adaptor sequences (CTGTCTCTTATACACA) were removed from the 5'-ends of both reads using preprocessReads, and truncated reads were further trimmed by one more base to allow for paired-end alignment to a reference mouse genome (GRCm38/mm10) with qAlign, which internally uses bowtie (Langmead et al., 2009). Around 70% of the obtained reads could be mapped. Peaks were identified on a pool of all samples using macs2 version 2.1.0.20140616 (Zhang et al., 2008) using parameters –nomodel

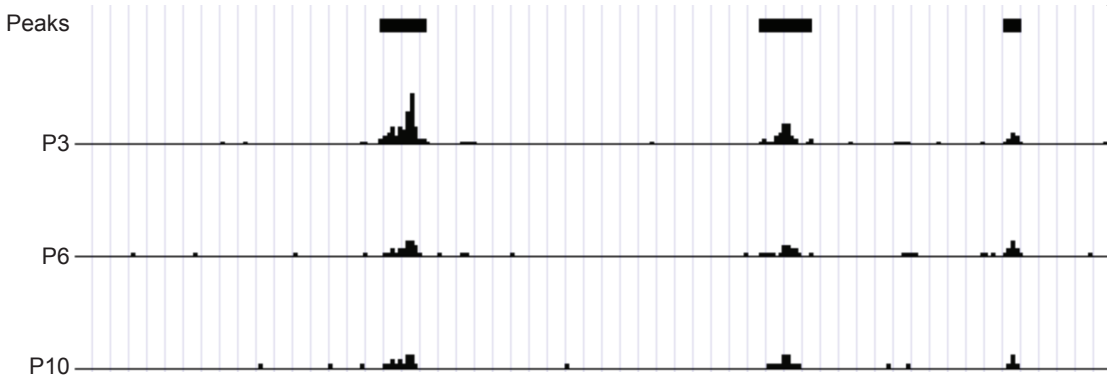

Figure 27. Example of ATACseq reads. ATACseq reqads at P3, P6, and P10 at a 27 kb intergenic region on chromosome 1. Identified peaks (using an algorithm from (Kim et al., 2016)) are marked with a black bar on the top. The first and second peak (from the left) lose accessibility before the switch (between P3 and P6) by 3- and 2-fold, respectively. They do not change significantly after the switch (between P6 and P10). The third peak's accessibility changes neither before nor after the switch.

–shift 0 –gsize 1.87e9 –qvalue 0.10 (Example in Figure 27). The number of reads in each sample was then quantified in these peak regions. Mean counts for each time point were determined and $\log_2$ transformed (adding 1 count to each value to avoid minus infinity values). Outliers were removed by removing the ten highest peaks. The nearest transcription start site was found using the transcript annotation from the package TxDb.Mmusculus.UCSC.mm10.knownGene. The glmQLFit model (Lund et al., 2012) from the edgeR package (McCarthy et al., 2012) was used to determine differential peaks. To compare our data to data from the literature (Mo et al., 2016), the regions of identified peaks in our data were chosen.

2.4.12 | Regularized regression model

The motif discovery analysis was done using an elastic net regression model (Friedman et al., 2010), as implemented in the glmnet package. The model predicts the

$\log_2$ fold changes of accessibility in ATAC-seq peaks as a linear combination of the number of predicted transcription factor binding sites in each peak (= region of accessible chromatin). The coefficients (beta) obtained when fitting the model are then interpreted as the importance of each transcription factor for the observed differences in accessibility. Transcription factor binding motifs for 519 vertebrate transcription factors were obtained from the JASPAR2016 Bioconductor package, and binding sites were predicted in ATACseq peaks using a $\log_2$-oods cutoff of 10.0, or the maximal score of the weight matrix if it was below that value. In order to control for differences in peak width and sequence composition, three additional predictors were added to the transcription factor binding sites: peak width, the number of G+C bases and the number of CpG dinucleotides. Due to the similarities in the binding motifs of different transcription factors and the resulting correlation between the numbers of predicted binding sites per peak, fitting a classical linear model could result in uninformative coefficients. The elastic net used here is a form of regularized linear regression that does not suffer from this situation: it adds two additional penalization terms to the optimization function (their relative weight is controlled by parameter alpha, and their total weight by parameter lambda), which results in the beta coefficients of correlated predictors to be shrunk towards each other. In addition, coefficients for less important predictors are shrunk towards zero, resulting in a sparse result in which only important predictors have non-zero coefficients. Optimal values for alpha and lambda were obtained by a grid search: for each possible value of alpha between 0 and 1 in steps of 0.1, the optimal value of lambda was obtained by 5-fold cross-validation as the value of lambda that resulted in the minimal mean squared error. Finally, the optimal combination of both parameters was selected that resulted in the overall

minimal mean squared error (alpha=0.4, lambda=5.169843e-5).

3 | Project 2 | Side project

Outer segment maintenance

miRNAs 182 & 183 Are Necessary to Maintain Adult Cone Photoreceptor Outer Segments and Visual Function

3.1 | Background

MicroRNAs (miRNAs) are posttranscriptional repressors of gene expression. Their biogenesis occurs in two steps. The primary RNA transcripts, pri-miRNAs, are cleaved by the Drosha/DGCR8 complex into pre-miRNAs, which are further processed by Dicer to become mature miRNAs (Krol et al., 2010). In animals, the majority of investigated miRNAs base pair imperfectly with messenger RNA (mRNA) sequences in the 3' UTR, which leads to translational repression, deadenylation, and degradation of target mRNAs.

The lack of all, or particular, miRNAs during development leads to various defects in the retina (Sundermeier and Palczewski, 2012), including retinal degeneration (Damiani et al., 2008; Lumayag et al., 2013; Zhu et al., 2011) or cone death (Sanuki et al., 2011). A set of miRNAs, the miRNAs in the miR-183/96/182 cluster, is mainly expressed in sensory neurons (Xu et al., 2007). Reduced activities

of these miRNAs leads to retinal degeneration (Zhu et al., 2011; Lumayag et al., 2013).

How do miRNAs contribute to the function of adult cones? To address this question, my colleagues developed a mouse model in which miRNA depletion occurs specifically in adult cones. We followed the subcellular structure, function, and gene expression in cones, and found two major changes. First, outer segments were lost and, therefore, light responses of cones were significantly reduced. Second, the genetic identity of cones, quantified by the expression of cone-specific genes, decreased significantly after miRNA depletion. Furthermore, we found that miRNAs of the miR-183/96/182 cluster accelerated the formation of inner segments, connecting cilia, and outer segments in retinal organoids.

3.2 | Results

3.2.1 | Depletion of miRNAs in adult cones leads to the loss of outer segments

To study how miRNA depletion affects adult cones, we used mice with a disrupted Drosha/DGCR8 miRNA-processing machinery. The Drosha/DGCR8 miRNA-processing machinery was genetically disrupted by crossing mice with conditional null Dgcr8 alleles (Yi et al., 2009) and mice expressing Cre recombinase postnatally specifically in cones (Le et al., 2004). The mouse line that is homozygous for the conditional null Dgcr8 allele and heterozygous for the Cre allele was crossed with a reporter mouse line (Madisen et al., 2010) conditionally expressing fluorescent tdTomato protein to reveal the morphology of cones. We call this mouse line C-DGCR-KO. Cones were examined in retinal sections and in retinal whole

mounts.

We detected Cre expression earliest at postnatal day 6 (P6). However, at P30, a time when the retina is fully developed, immunohistochemistry revealed no appreciable difference in DGCR8 signal between C-DGCR-KO and wild-type cone nuclei (Figure 1 and Figure 2). The slow depletion of DGCR8 protein (and consequently the miRNAs) is likely due to its high stability. DGCR8 stability is known to be modulated by its phosphorylation and interactions with other proteins (Cheng et al., 2014; Han et al., 2009; Herbert et al., 2013): these phenomena possibly also stabilize the protein in cones.

At P30, cone morphology and opsin-labeled (OPN1SW and OPN1MW) outer segment distribution in whole-mount retinas assayed by immunohistochemistry was similar in C-DGCR-KO and wild-type mice (Figures Figure 3). The observation that adult cones of C-DGCR-KO mice at P30 had a normal structure (Figure 4), indicated a proper development and maturation of cone photoreceptors and allowed us to investigate the effect of progressive loss of mature miRNAs in adult cones.

In contrast to P30, DGCR8 immunostaining in cone nuclei was not detectable in retinal sections at P60 (Figure 5). Moreover, miRNA levels were 95% lower than in wild-type cones. Hence, at P60 the DGCR8 function was largely lost and, consequently, miRNAs were depleted from cones. Importantly, in this miRNA-depleted cone state, we found that the number of cone outer segments labeled with cone opsins was reduced by 90% (Figure 7 and Figure 6). Since the number of cones counted in whole-mount retinas was similar in C-DGCR-KO and wild-type mice (Figure 8), the loss of opsin staining was not due to the death of cones.

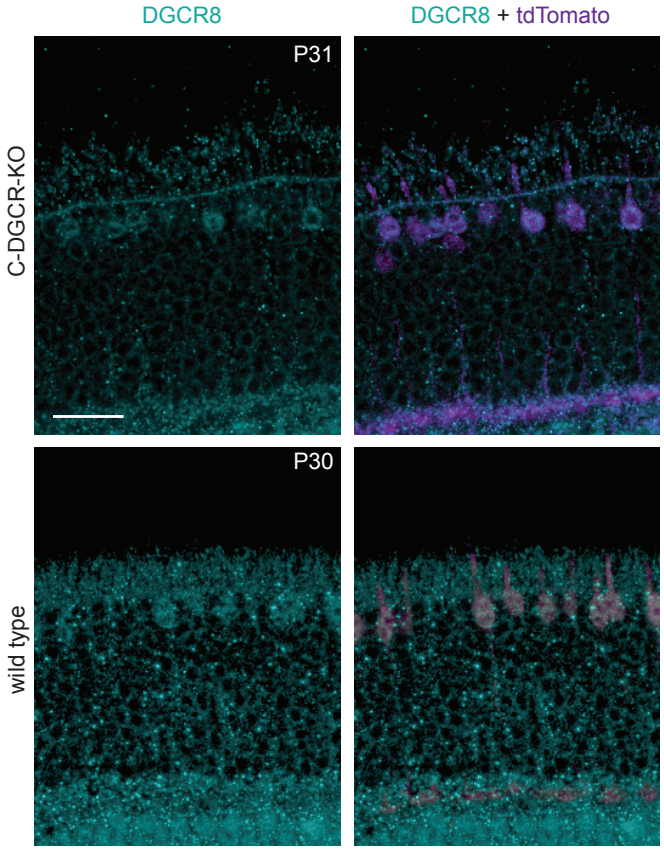

Figure 1. DGCR8 expression in C-DGCR8-KO retinas is similar to wild type retinas. Cross sections of DGCR8- (cyan) and tdTomato-labeled (magenta) cones in C-DGCR-KO (upper row) and wild type (bottom row) retinas at time points indicated. Scale bar 20 µm.

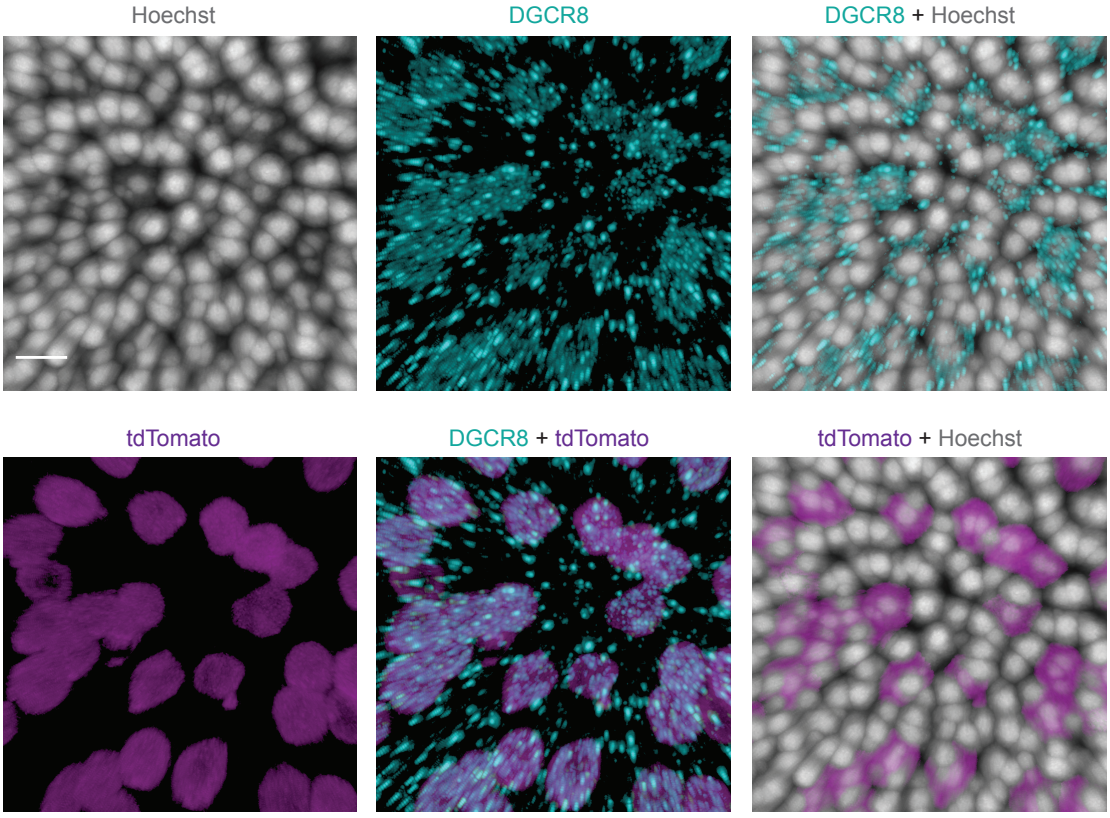

Figure 2. DGCR8 staining is enriched in cone nuclei. Confocal images of a section showing cone and rod photoreceptor cell bodies and nuclei in a wild type P60 retina. The retina was stained with antibodies against DGCR8 (cyan) and tdTomato (magenta; visualizing cones), and Hoechst (white) staining nuclei. Different merged staining are shown. Scale bar 4 µm.

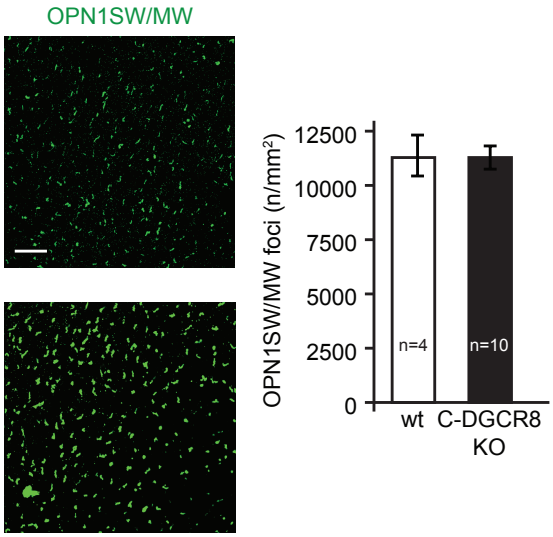

Figure 3. Cones of P30 C-DGCR-KO mice have not yet lost their outer segments. Confocal microscopy images of C-DGCR-KO (top row) and wild-type (bottom row) wholemount retinas, OPN1SW/MW signal in green. Scale bar 20 µm.

3.2.2 | Mechanism of miRNA mediated maintenance of outer segments and implications for retinal organoids

This part has mostly been done by my coworkers and is briefly summarized here to give a complete picture of the study.

Outer segments and opsin expression are important for light detection. We therefore tested the ability of the P60 C-DGCR-KO retina to respond to light stimuli in vivo and ex vivo and found reduced light responses.

To reveal fine morphological changes in the P60 opsin-less cones, we reconstructed the outer retina of P30 and P60 C-DGCR-KO and of P60 wild-type mice using 3D EM. All P60 C-DGCR-KO cones lacked outer segments. To determine the time course of outer segment loss, we 3D-reconstructed the outer retina at P30, P40, P50, and P60. At P30, C-DGCR8-KO cone outer segments had similar

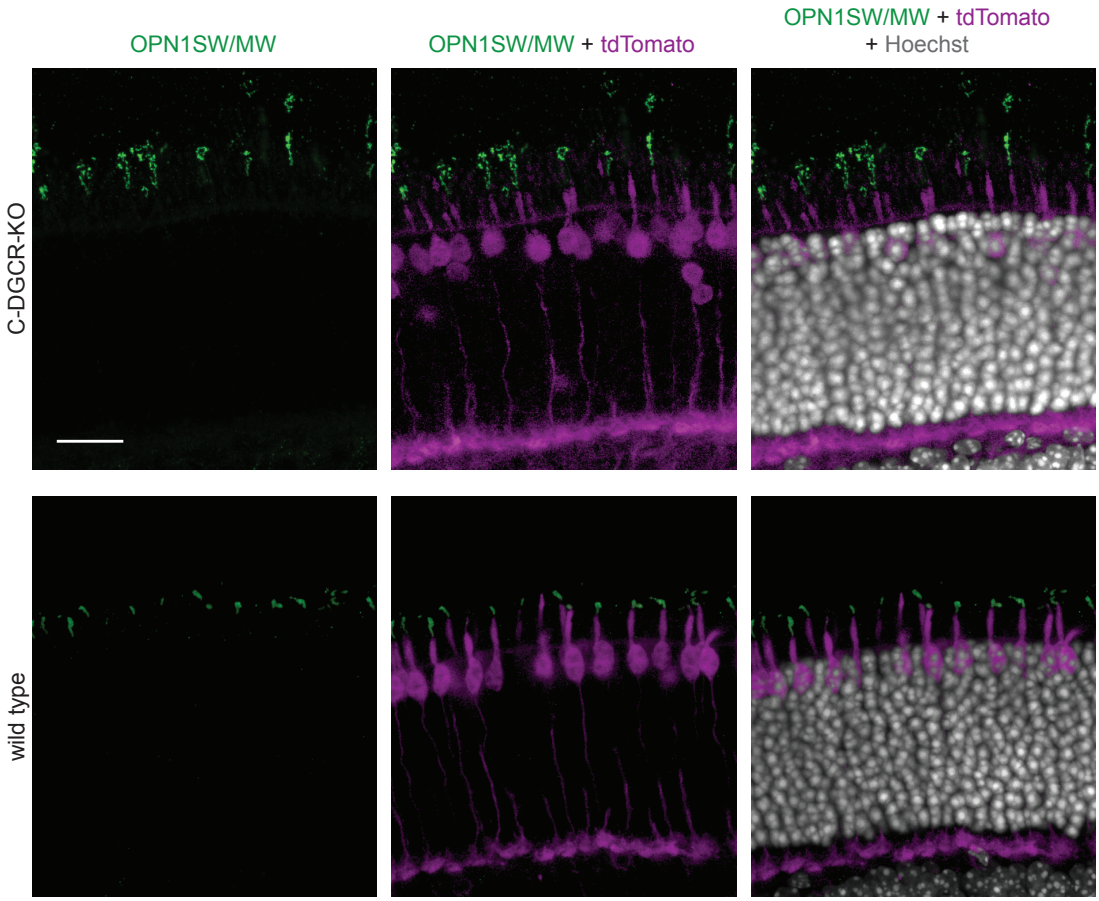

Figure 4. Cones of P30 C-DGCR-KO mice have a similar morphology as wild type cones. Cross-sections of C-DGCR-KO (top row) and wild-type (bottom row) retinas immunostained for OPN1SW/MW (green), merged with tdTomato-labeled cones (magenta), and additionally merged with Hoechst dye stained nuclei (white). Scale bar 20 µm.

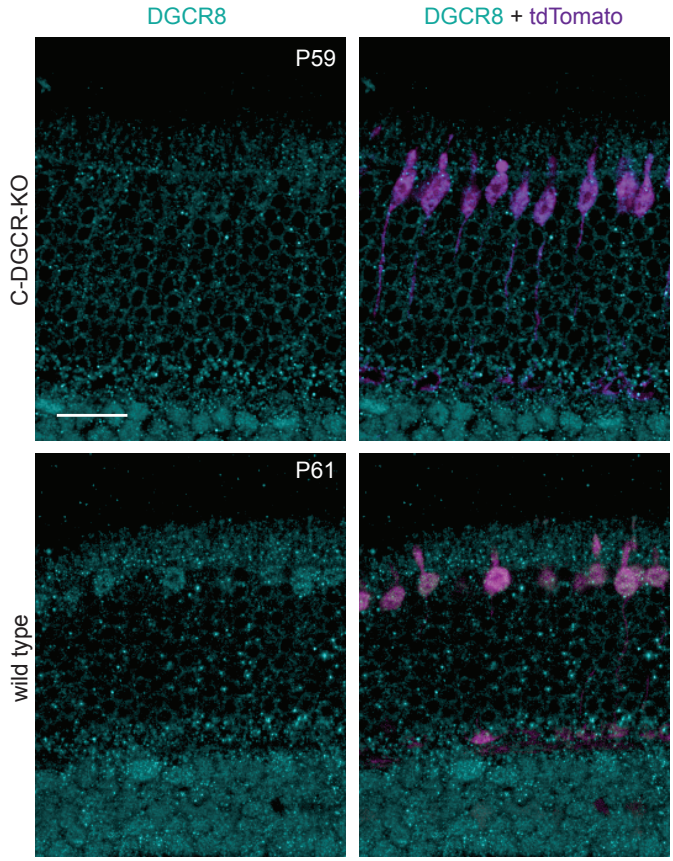

Figure 5. Reduced DGCR8 expression in C-DGCR8-KO mice at P60. Cross sections of DGCR8 (cyan) and tdTomato-labeled (magenta) cones in C-DGCR-KO (upper row) and wild type (bottom row) retinas at time points indicated. Scale bar 20 µm.

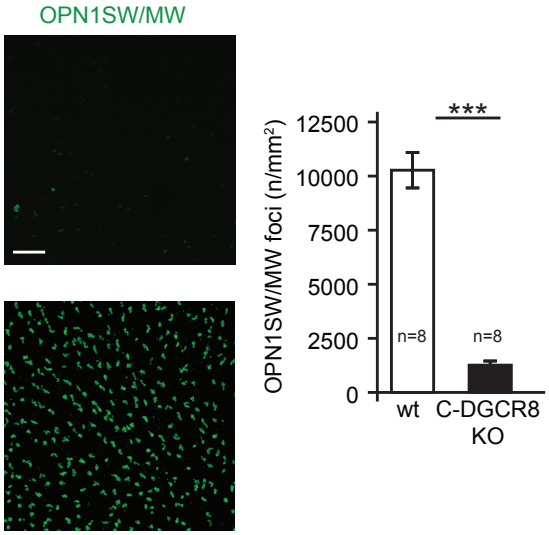

Figure 6. Cones of P60 C-DGCR-KO mice have lost their outer segments. Confocal microscopy images of C-DGCR-KO (top row) and wild-type (bottom row) wholemount retinas, OPN1SW/MW signal in green. Scale bar 20 µm.

lengths to wild-type, but at subsequent time points they shortened in a linear fashion until they became undetectable at P60.

Re-expression of the sensory-cell-specific miR-182 and miR-183 in cones at P30 prevented outer segment loss at P60. This shows that miR-182 and miR-183 are sufficient for the maintenance of outer segments.

RNA sequencing of isolated cones at P30, P40, P50, P60, and P90 revealed that most genes remain expressed at similar levels. 96.7% of the expressed genes changed less than 2-fold. Genes from the phototransduction pathway were significantly downregulated, whereas genes related to synaptic transmission were not affected significantly. One third of cone-specific genes had been significantly downregulated. Among upregulated and predicted miR-182 and miR-183 targets there were genes related to membrane trafficking, lipid metabolism, and cilium formation. Thus, depletion of miRNAs leads to the gradual loss of the genetic identity

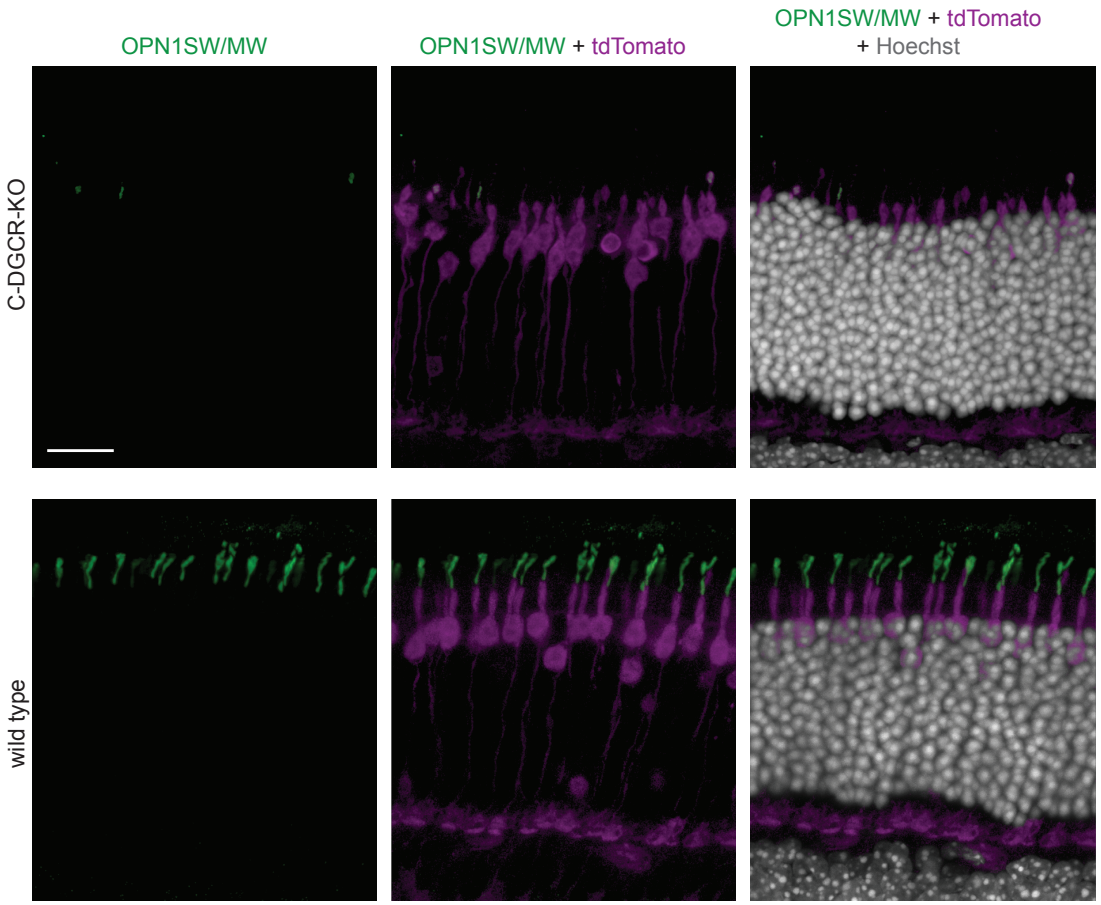

Figure 7. Cones of P60 C-DGCR-KO mice have lost their outer segments Cross-sections of C-DGCR-KO (top row) and wild-type (bottom row) retinas immunostained for OPN1SW/MW (green), merged with tdTomato-labeled cones (magenta), and additionally merged with Hoechst dye stained nuclei (white).Scale bar 20 µm.

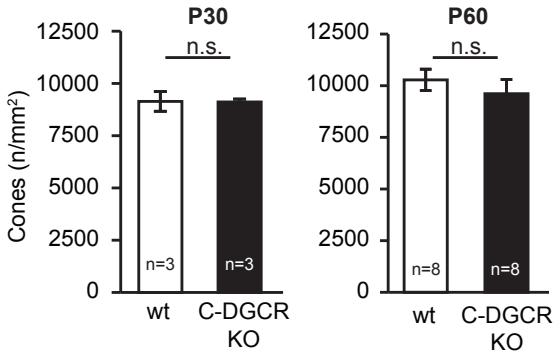

Figure 8. Number of cone nuclei. The number of cone nuclei per mm^2 is not significantly different in wild-type and C-DGCR8-KO mice.

of cones.

In retinal organoids, no outer segments have been detected before (Gonzalez-Cordero et al., 2013). Expressing miR-182 and miR-183 in retinal organoids showed that they were necessary and sufficient for the formation of inner segments, connecting cilia and short outer segments, as well as light responses in retinal organoids.

3.3 | Discussion

Our results show that miR-182- and miR-183-regulated pathways are necessary for cone outer segment maintenance in vivo and functional outer segment formation in vitro. Using an in vivo model system that we set up to study the role of miRNAs in mature cones, we found that the depletion of miRNAs, resulting from the knockout of DGCR8 in adult cones, led to the loss of outer segments. The outer segment loss was prevented by re-expression of miR-182 and miR-183, suggesting that these miRNAs are important for the maintenance of outer segments.

We found a gradual loss of outer segments as the miRNA levels decreased

between P30 and P60, without any change in the number of cones or any systematic increase in proapoptotic gene expression.

We found that expression of Arr3 and Opn1mw and other phototransduction genes decreased between P30 and P60. Interestingly, the decrease was not limited to the phototransduction cascade genes but also applied to many other genes known to be specifically expressed in cones. Therefore, it appears that in the absence of miR-182 and miR-183, cones largely lose their genetic signature, i.e., the expression of cell-type-specific genes. This change in gene expression was delayed compared to the shortening of outer segments, and it is therefore unlikely that the outer segment loss is due to the aforementioned general decrease in cone-specific gene expression. It is possible that the loss of outer segments induces a feedback signal to the nucleus that reduces the expression of cone-specific genes. Alternatively, these two phenotypes are independent from eachother.

Using an in vitro model system, stem-cell-derived retinal organoids, we found that the miR-183/96/182 cluster miRNAs were necessary and sufficient for the formation of inner segments, connecting cilia and short outer segments, as well as light-induced hyperpolarization.

The miR-183/96/182 cluster is needed for the maintenance of cone outer segments in vivo, and for the formation of inner segments, connecting cilia, and outer segments in retinal organoids in in vitro. Both of these functions could be explained if the effect of the cluster miRNAs is to optimize the supply of molecular components for the assembly of distal photoreceptor structures. The outer segments of both rods and cones are dynamically maintained in adults: the pigment epithelial cells phagocytize the distal membrane disks, and the proximal disks are continuously renewed by the photoreceptors. In adult C-DGCR8-KO cones, a re-

duced supply of essential outer segment components would lead to an imbalance between the pace of phagocytosis at the distal tip and the formation of new outer segment membrane and protein components at the base of the outer segment. The continued phagocytosis and suboptimal regeneration would lead to a shortening of the outer segments. Similarly, in photoreceptors developing in vitro, miRNAs of the miR-183/96/182 cluster might control the supply of components to the apical membrane, accelerating the formation of distal structures. Among the upregulated and predicted targets of miR-182 and miR-183 were many genes involved in membrane trafficking, lipid metabolism, and cilium formation pathways. To explain the shortening of the outer segments, one would predict an overall decrease or misregulation in membrane flow toward the distal tip of cones. The increased expression of genes encoding proteins that activate endocytosis provides a possible explanation of a deficiency in membrane flow.

The miR-183/96/182 cluster is also expressed in other sensory organs, not just the retina (Xu et al., 2007). In hair cells of the inner ear, the miR-183/96/182 cluster miRNAs are expressed in a gradient: high on the apical side and low on the basal side of the cochlea (Groves et al., 2013; Soukup, 2009). Correlating with this miRNA gradient, the distal structures of hair cells, including the cilium bundle, are longer on the apical than the basal side, and in the Dicer knockout mouse model the residual miR-183/96/182 cluster expression correlates with the extent of hair bundle length (Soukup, 2009). Therefore, the "increased supply" mechanism proposed above for retinal photoreceptors may also apply to hair cells.

3.4 | Methods

3.4.1 | Animals

All animal experiments and procedures were approved by the Swiss Veterinary Office. The animals were maintained under a 12 hr light-dark cycle. Conditional DGCR8 knockout mice (Yi et al., 2009) were crossed to the cone photoreceptor-specific Cre recombinase driver line D4-cre (Le et al., 2004), resulting in C-DGCR-KO mice. In D4-Cre line the human red/green opsin promoter drives expression of Cre in cones. To visualize cones, we further crossed C-DGCR-KO mice to the floxed tdTomato reporter line Ai9 (Madisen et al., 2010) (JAX mice B6.Cg-Gt(ROSA)26Sor$^{tm9(CAG\text{-}tdTomato)Hze}$/J, Stock Number 007909, Jackson Laboratory). D4-cre or D4-cre/Ai9 animals served as wild-type controls.

3.4.2 | Immunohistochemistry

Immunohistochemistry was performed as previously described (Busskamp et al., 2010). Mouse retinas or retinas grown from ES cells were isolated and fixed in 4% paraformaldehyde in phosphate-buffered saline (PBS) for 20 min and washed in PBS. Retinal wholemounts or 3% agarose-embedded (SeaKem Le Agarose, Lonza) 100 µm thick vibratome sections (Leica VT1000S vibratome) were incubated in blocking solution (10% normal donkey serum (NDS, Chemicon), 1% bovine serum albumin (BSA), and 0.5% Triton X-100 in PBS, pH 7.4) for 1 h. Primary and secondary antibody applications were done in 3% NDS, 1% BSA, 0.02% sodium azide, and 0.5% Triton X-100 in PBS. Primary antibodies were applied for approximately 4 days. Specimens were mounted on a glass slide with ProLong Gold antifade reagent (Invitrogen). As primary antibodies we used goat-

anti-OPN1SW (1:200, Santa Cruz, sc- 14365), goat-anti-OPN1MW/LW (1:200, Santa Cruz, sc-22117), rabbit-anti-DGCR8 (1:200, Bethyl, A302-469A), sheep-anti-CHX10 (1:400, Exalpha, X2398M), rabbit-anti-Recoverin (1:400, Chemicon, AB5585), rabbit-anti-PRPH2 (Peripherin) (1:200, Proteintech Group), and mouse-anti-Rhodopsin (1:800, Sigma, 5403). As secondary antibodies, donkey-anti-goat-Alexa488 (1:200, Invitrogen, A11055), donkey-anti-rabbit-Alexa647 (1:200, Invitrogen, A315773), donkey-anti-sheep-Alexa488 (1:200, Invitrogen, A11015), donkey-anti-rabbit-Alexa568 (1:200, Invitrogen, A10042), and donkey-anti-mouse-Alexa647 (1:200, Invitrogen, A31571) were used. Nuclei were stained with the dye Hoechst (1:600, Invitrogen, H3570, 10 mg/ml). TdTomato signal persisted fixation and staining steps.

3.4.3 | Confocal microscopy

A Zeiss LSM 700 laser scanning confocal microscope was used to acquire images of antibody-stained retinas with an EC Plan-Neofluar 40×/1.30 oil M27 objective. Morphologies of the cones were assessed from 1024×1024 pixel images in a z-stack with 1 µm z-steps. Images were processed using Imaris (Bitplane) or Fiji.

3.4.4 | Electron microscopy

Retinas were fixed with 2% paraformaldehyde and 2% glutaraldehyde in 0.1 M Na-cacodylate buffer, pH 7.4, and embedded in 4% agarose. Retinas were cut in 60 µm coronal vibratome sections in PBS and processed according to a modified version of the NCMIR protocol (ncmir.ucsd.edu/sbfsem-protocol.pdf). Sections were collected and rinsed 3×5 min with 0.1 M Na-cacodylate buffer, pH 7.4, and post-fixed with 1.5% potassium ferrocyanide and 1% osmium tetroxide in 0.1 M

Na-cacodylate buffer for 30 min. After rinsing in ddH_2O, sections were stained in 1% thiocarbohydrazide for 10 min. After rinsing, sections were immersed in 1% osmium tetroxide for 20 min. Following extensive rinsing in ddH_2O, sections were stained en bloc with 1% aqueous uranyl acetate overnight at 4 °C. The following day, sections were dehydrated with ethanol and flat-embedded in Epon resin (Serva). After 24 h of curing in an oven at 60 °C, sections were screened under a light microscope and the region of interest selected. For serial block-face scanning electron microscopy (SBEM), the region of interest was cut out of the flat-embedded section and mounted perpendicularly on a pin suitable for serial block-face scanning electron microscope (3View from GATAN in an FEI QUANTA 200 VP_FEG scanning electron microscope) in order to have the photoreceptors at the top of the block. The tissue was then trimmed and placed in the microscope. The surface of the block was imaged (3.5 kV, spot size 3, 4000×4000 pixels, 12 nm/pixel, 5 ms dwell time) and then 80 or 100 nm was shaved from the surface using a diamond knife before the new surface was imaged. Stacks of 700-1200 images were acquired. Images were then exported in TIF format and registered (translation-rotation) using the TrackEM2 registration procedure. The final images were then exported in TIF format.

3.4.5 | Image analysis

Confocal microscopy images were quantified using the automatic cell-counting feature (Spots) in Imaris 7.6 (Bitplane). The number of cone photoreceptors was determined by counting tdTomato-positive or peanut agglutinin lectin-Alexa Fluor 568 conjugate (Molecular Probes, L-32458) labeled cells. Electron microscope image stacks were analyzed using Fiji software. The EM images were 12 nm (x) ×

12 nm (y) $\times$ 100 nm (depth). The length of the cone outer segments was defined by the length of the electrodense material in the outer segment representing the disk membrane.

4 | Conclusion

The aim of my PhD thesis was to understand how the eye's light-sensors form and how they are maintained.

By correlating the ultrastructure and gene expression of developing cones, I found a major switch in cone morphology and gene expression. The switch occurs at P6 and involves 14% of all genes expressed in cones. Intriguingly, the switch coincides with the formation of cone outer segments. Pathways essential for establishing a functional cone switch on, while components of general neuronal development switch off. The switch is mostly regulated transcriptionally, and is preceded by a genome-wide loss in chromatin accessibility. The chromatin accessibility loss mostly affected enhancer elements – particularly regions without CTCF binding sites.

Further, I was involved in showing that the disruption of DGCR8 in adult cones leads to the loss of outer segments. Based on that finding, my coworkers found that miR-182- and miR-183-regulated pathways are necessary for cone outer segment maintenance in vivo and functional outer segment formation in vitro in retinal organoids.

My results might contribute to understanding how to prevent or repair sensory loss. The loss of cone outer segments is a common outcome for a number of retinal diseases and can lead to blindness. The finding that outer segment formation

involves gene expression switch that is preceded by a genome-wide chromatin accessibility loss provides a possible direction for future investigations of blindness conditions. It would be insightful to study if photoreceptors in certain blindness diseases show altered gene expression and chromatin accessibility that is comparable to the pre-switch state (before P6) of cone photoreceptors. If so, then finding ways to induce the post-switch state (after P6) would be desirable. In spinocerebellar ataxia type 7 (SCA7), photoreceptors are affected severely, which leads to retinal degeneration and blindness (Helmlinger et al., 2006). Initially, only cone photoreceptors are affected and the diesease progress towards a cone-rod dystrophy (La Spada et al., 2001). In mouse models for SCA7, many genes that are photoreceptor-specific and involved in the phototransduction cascade are down-regulated strongly at early stages of the disease (Abou-Sleymane et al., 2006; La Spada et al., 2001; Yoo et al., 2003). This is similar to the pre-switch state in developing photoreceptors. Interestingly, chromatin is also strongly decondensed in photoreceptors of mouse models for SCA7, and photoreceptor dysfunction correlated with the degree of decondensation (Helmlinger et al., 2006). Thus, linking the results presented in this thesis with SCA7 research might open new avenues for a better understanding of that disease. A possible direction is to study how CTCF is involved in the switch because the gene (ataxin-7) whose mutation causes SCA7 was found to be regulated by CTCF (Sopher et al., 2012).

It would further be interesting to assess whether ES- or iPSC-derived retinal organoids ondergo a gene expression switch and chromatin re-organization comparable to the developing retina at P6. If so then knowing the timepoint at which it occurs could help to reduce variability in organoid experiments – one of the major challenges in organoid research (Fatehullah et al., 2016). If the switch is present in

retinal organoids, a set of markers could be defined to determine the maturation state of an organoid. If the switch is absent or incomplete in retial organoids, that provides a direction for research aiming at inducing outer segments at a large scale in organoids.

The finding that miR-183/96/182 cluster expression leads to the induction of outer segments in ES-cell-derived retinal organoids, and that the same cluster is downregulated in several mouse models of the blinding disease retinitis pigmentosa (Loscher et al., 2008), suggests that reexpression of these miRNAs, either alone or in combination with other factors that keep cones alive (Leveillard and Sahel, 2010; Punzo et al., 2009; Li et al., 2010) could be a potential strategy for outer segment regeneration.

5 | Bibliography

Gretta Abou-Sleymane, Frederic Chalmel, Dominique Helmlinger, Aurelie Lardenois, Christelle Thibault, Chantal Weber, Karine Merienne, Jean Louis Mandel, Olivier Poch, Didier Devys, and Yvon Trottier. Polyglutamine expansion causes neurodegeneration by altering the neuronal differentiation program. *Human Molecular Genetics*, 15(5):691–703, 2006. ISSN 09646906. doi: 10.1093/hmg/ddi483.

Allen Brain Atlas. Allen Brain Atlas, 2016. URL http://mouse.brain-map.org/.

Kin Fai Au, Hui Jiang, Lan Lin, Yi Xing, and Wing Hung Wong. Detection of splice junctions from paired-end RNA-seq data by SpliceMap. *Nucleic Acids Research*, 38(14):4570–4578, 2010. ISSN 13624962. doi: 10.1093/nar/gkq211.

Tomer Avidor-Reiss, Andreia M. Maer, Edmund Koundakjian, Andrey Polyanovsky, Thomas Keil, Shankar Subramaniam, and Charles S. Zuker. Decoding Cilia Function. *Cell*, 117(4):527–539, 2004. ISSN 00928674. doi: 10.1016/S0092-8674(04)00412-X.

William B. Barkis, Kevin J. Ford, and Marla B. Feller. Non-cell-autonomous factor induces the transition from excitatory to inhibitory GABA signaling in retina independent of activity. *Proc Natl Acad Sci U S A*, 107(51):22302–22307, 2010.

ISSN 1091-6490. doi: 10.1073/pnas.1008775108. URL http://www.ncbi.nlm.nih.gov/pubmed/21135238.

Joseph A. Brzezinski and Thomas A. Reh. Photoreceptor cell fate specification in vertebrates. *Development*, 142(19):3263–3273, 2015. ISSN 0950-1991. doi: 10.1242/dev.127043. URL http://www.ncbi.nlm.nih.gov/pubmed/26443631.

Jason D. Buenrostro, Paul G. Giresi, Lisa C. Zaba, Howard Y. Chang, and William J. Greenleaf. Transposition of native chromatin for fast and sensitive epigenomic profiling of open chromatin, DNA-binding proteins and nucleosome position. *Nature Methods*, 10(12):1213–1218, dec 2013. ISSN 1548-7091. doi: 10.1038/nmeth.2688. URL http://www.nature.com/doifinder/10.1038/nmeth.2688http://dx.doi.org/10.1038/nmeth.2688.

Volker Busskamp, Jens Duebel, David Balya, Mathias Fradot, Tim J. Viney, Sandra Siegert, Anna C. Groner, Eric Cabuy, Valerie Forster, Mathias Seeliger, Martin Biel, Peter Humphries, Michel Paques, Saddek Mohand-Said, Didier Trono, Karl Deisseroth, Jose A. Sahel, Serge Picaud, and Botond Roska. Genetic reactivation of cone photoreceptors restores visual responses in retinitis pigmentosa. *Science*, 329 (5990):413–417, 2010. ISSN 0036-8075. doi: 10.1126/science.1190897. URL http://www.ncbi.nlm.nih.gov/pubmed/20576849{%}5Cnhttp://science.sciencemag.org/content/329/5990/413.long.

Volker Busskamp, Jacek Krol, Dasha Nelidova, Janine Daum, Tamas Szikra, Ben Tsuda, Josephine Jüttner, Karl Farrow, Brigitte Gross Scherf, Claudia Patricia Patino Alvarez, Christel Genoud, Vithiyanjali Sothilingam, Naoyuki Tani-

moto, Michael Stadler, Mathias Seeliger, Markus Stoffel, Witold Filipowicz, and Botond Roska. MiRNAs 182 and 183 Are Necessary to Maintain Adult Cone Photoreceptor Outer Segments and Visual Function. *Neuron*, 83(3):586–600, 2014a. ISSN 10974199. doi: 10.1016/j.neuron.2014.06.020.

Volker Busskamp, Nathan E. Lewis, Patrick Guye, Alex H. Ng, Seth L. Shipman, Susan M. Byrne, Neville E. Sanjana, Jernej Murn, Yinqing Li, Shangzhong Li, Michael Stadler, Ron Weiss, and George M. Church. Rapid neurogenesis through transcriptional activation in human stem cells. *Mol Syst Biol*, 10(760), 2014b. ISSN 1744-4292. doi: 10.15252/msb.20145508. URL http://www.ncbi.nlm.nih.gov/pubmed/25403753.

Albert Cardona, Stephan Saalfeld, Johannes Schindelin, Ignacio Arganda-Carreras, Stephan Preibisch, Mark Longair, Pavel Tomancak, Volker Hartenstein, and Rodney J. Douglas. TrakEM2 software for neural circuit reconstruction. *PLoS ONE*, 7(6), 2012. ISSN 19326203. doi: 10.1371/journal.pone.0038011.

Louvenia D. Carter-Dawson and Matthew M. LaVail. Rods and cones in the mouse retina. I. Structural analysis using light and electron microscopy. *The Journal of comparative neurology*, 188(2):245–62, 1979. ISSN 0021-9967. doi: 10.1002/cne.901880204. URL http://www.ncbi.nlm.nih.gov/pubmed/500858.

Tian Lin Cheng, Zhizhi Wang, Qiuming Liao, Ying Zhu, Wen Hao Zhou, Wenqing Xu, and Zilong Qiu. MeCP2 Suppresses Nuclear MicroRNA Processing and Dendritic Growth by Regulating the DGCR8/Drosha Complex. *Developmental Cell*, 28(5):547–560, 2014. ISSN 18781551. doi: 10.1016/j.devcel.2014.01.032.

Devid Damiani, John J. Alexander, Jason R. O'Rourke, Mike McManus, Ashutosh P. Jadhav, Constance L. Cepko, William W. Hauswirth, Brian D. Harfe, and Enrica Strettoi. Dicer inactivation leads to progressive functional and structural degeneration of the mouse retina. *The Journal of neuroscience : the official journal of the Society for Neuroscience*, 28(19):4878–4887, 2008. ISSN 0270-6474. doi: 10.1523/JNEUROSCI.0828-08.2008.

Winfried Denk and Heinz Horstmann. Serial block-face scanning electron microscopy to reconstruct three-dimensional tissue nanostructure. *PLoS Biology*, 2(11), 2004. ISSN 15449173. doi: 10.1371/journal.pbio.0020329.

Bettie Duncan and Ann Christopher Herald. Some Observations on the Ultrastructure of Epicoccum nigrum. *Mycologia*, 66(6):1022–1029, 1974.

MarkM Emerson, Natalia Surzenko, JillianJ Goetz, Jeffrey Trimarchi, and ConstanceL Cepko. Otx2 and Onecut1 promote the fates of cone photoreceptors and horizontal cells and repress rod photoreceptors. *Developmental Cell*, 26 (1):59–72, 2013. ISSN 15345807. doi: 10.1016/j.devcel.2013.06.005. URL http://dx.doi.org/10.1016/j.devcel.2013.06.005.

Aliya Fatehullah, Si Hui Tan, and Nick Barker. Organoids as an in vitro model of human development and disease. *Nat Cell Biol*, 18(3):246–254, 2016. ISSN 1465-7392. doi: 10.1038/ncb3312. URL http://dx.doi.org/10.1038/ncb3312{%}5Cn10.1038/ncb3312.

Jerome Friedman, Trevor Hastie, and Rob Tibshirani. Regularization Paths for Generalized Linear Models via Coordinate Descent. *Journal of Statistical Software*, 33(1), 2010.

Dimos Gaidatzis, Anita Lerch, Florian Hahne, and Michael B. Stadler. QuasR: Quantification and annotation of short reads in R. *Bioinformatics*, 31(7):1130–1132, 2015. ISSN 14602059. doi: 10.1093/bioinformatics/btu781.

Riki Gibson, Erica L. Fletcher, Algis J. Vingrys, Yuan Zhu, Kirstan A. Vessey, and Michael Kalloniatis. Functional and neurochemical development in the normal and degenerating mouse retina. *Journal of Comparative Neurology*, 521(6):1251–1267, 2013. ISSN 00219967. doi: 10.1002/cne.23284.

Anai Gonzalez-Cordero, Emma L. West, Rachael A. Pearson, Yanai Duran, Livia S. Carvalho, Colin J. Chu, Arifa Naeem, Samuel J. I. Blackford, Anastasios Georgiadis, Jorn Lakowski, Mike Hubank, Alexander J. Smith, James W. B. Bainbridge, Jane C. Sowden, and Robin R. Ali. Photoreceptor precursors derived from three- dimensional embryonic stem cell cultures integrate and mature within adult degenerate retina. *Nature Biotechnology*, 31 (8):741–747, 2013. ISSN 1087-0156. doi: 10.1038/nbt.2643. URL http://dx.doi.org/10.1038/nbt.2643.

Andrew K. Groves, Kaidi D. Zhang, and Donna M. Fekete. The genetics of hair cell development and regeneration. *Annual review of neuroscience*, 36: 361–81, 2013. ISSN 1545-4126. doi: 10.1146/annurev-neuro-062012-170309. URL http://www.annualreviews.org.proxy.lib.duke.edu/doi/full/10.1146/annurev-neuro-062012-170309.

Jinju Han, Jakob S. Pedersen, S. Chul Kwon, Cassandra D. Belair, Young Kook Kim, Kyu Hyeon Yeom, Woo Young Yang, David Haussler, Robert Blelloch, and V. Narry Kim. Posttranscriptional Crossregulation between Drosha and

DGCR8. *Cell*, 136(1):75–84, 2009. ISSN 00928674. doi: 10.1016/j.cell.2008.10.053.

Dominique Helmlinger, Laszlo Tora, and Didier Devys. Transcriptional alterations and chromatin remodeling in polyglutamine diseases, 2006. ISSN 01689525.

Kristina M. Herbert, Genaro Pimienta, Suzanne J. DeGregorio, Andrei Alexandrov, and Joan A. Steitz. Phosphorylation of DGCR8 Increases Its Intracellular Stability and Induces a Progrowth miRNA Profile. *Cell Reports*, 5(4):1070–1081, 2013. ISSN 22111247. doi: 10.1016/j.celrep.2013.10.017.

Christine E. Holt, Thomas W. Bertsch, Hilary M. Ellis, and William A. Harris. Cellular determination in the xenopus retina is independent of lineage and birth date. *Neuron*, 1(1):15–26, 1988. ISSN 08966273. doi: 10.1016/0896-6273(88)90205-X.

Ravi S. Jonnal, Jason R. Besecker, Jack C. Derby, Omer P. Kocaoglu, Barry Cense, Weihua Gao, Qiang Wang, and Donald T. Miller. Imaging outer segment renewal in living human cone photoreceptors. *Optics express*, 18(5):5257–70, 2010. ISSN 1094-4087. doi: 10.1364/OE.18.005257. URL http://www.ncbi.nlm.nih.gov/pubmed/20389538{%}5Cnhttp://www.pubmedcentral.nih.gov/articlerender.fcgi?artid=PMC3113600.

Jung-Woong Kim, Hyun-Jin Yang, Matthew John Brooks, Lina Zelinger, Gökhan Karakülah, Norimoto Gotoh, Alexis Boleda, Linn Gieser, Felipe Giuste, Dustin Thad Whitaker, Ashley Walton, Rafael Villasmil, Jennifer Joanna Barb, Peter Jonathan Munson, Koray Dogan Kaya, Vijender Chaitankar, Tiziana Cogliati, and Anand Swaroop. NRL-Regulated Transcriptome Dynam-

ics of Developing Rod Photoreceptors. *Cell Reports*, 17(9):2460–2473, 2016. ISSN 22111247. doi: 10.1016/j.celrep.2016.10.074. URL http://linkinghub.elsevier.com/retrieve/pii/S2211124716315091.

Jacek Krol, Inga Loedige, and Witold Filipowicz. The widespread regulation of microRNA biogenesis, function and decay. *Nature reviews. Genetics*, 11(9):597–610, 2010. ISSN 1471-0056. doi: 10.1038/nrg2843. URL http://dx.doi.org/10.1038/nrg2843.

Albert R. La Spada, Ying Hui Fu, Bryce L. Sopher, Randell T. Libby, Xuejiao Wang, Lili Y. Li, David D. Einum, Jing Huang, Daniel E. Possin, Annette C. Smith, Refugio A. Martinez, Kari L. Koszdin, Piper M. Treuting, Carol B. Ware, James B. Hurley, Louis J. Ptáček, and Shiming Chen. Polyglutamine-expanded ataxin-7 antagonizes CRX function and induces cone-rod dystrophy in a mouse model of SCA7. *Neuron*, 31(6):913–927, 2001. ISSN 08966273. doi: 10.1016/S0896-6273(01)00422-6.

Ben Langmead, Cole Trapnell, Mihai Pop, and Steven L. Salzberg. Ultrafast and memory-efficient alignment of short DNA sequences to the human genome. *Genome Biol.*, 10(3):R25, 2009. ISSN 1465-6914. doi: 10.1186/gb-2009-10-3-r25.

Yun-Zheng Le, John D. Ash, Muayyad R. Al-Ubaidi, Ying Chen, Jian-Xing Ma, and Robert E. Anderson. Targeted expression of Cre recombinase to cone photoreceptors in transgenic mice. *Molecular vision*, 10:1011–8, 2004. ISSN 1090-0535. doi: v10/a120[pii]. URL http://www.ncbi.nlm.nih.gov/pubmed/15635292.

Thierry Leveillard and Jose A. Sahel. Rod-derived cone viability factor for treating blinding diseases: from clinic to redox signaling. *Sci Transl Med*, 2(26):26ps16, 2010. ISSN 1946-6234. doi: 10.1126/scitranslmed.3000866. URL http://www.ncbi.nlm.nih.gov/pubmed/20375363.

Yiwen Li, Weng Tao, Lingyu Luo, Deqiang Huang, Konrad Kauper, Paul Stabila, Matthew M. Lavail, Alan M. Laties, and Rong Wen. CNTF induces regeneration of cone outer segments in a rat model of retinal degeneration. *PLoS ONE*, 5(3), 2010. ISSN 19326203. doi: 10.1371/journal.pone.0009495.

Carol J. Loscher, Karsten Hokamp, John H. Wilson, Tiansen Li, Peter Humphries, G. Jane Farrar, and Arpad Palfi. A common microRNA signature in mouse models of retinal degeneration. *Experimental Eye Research*, 87(6):529–534, 2008. ISSN 00144835. doi: 10.1016/j.exer.2008.08.016.

Stephen Lumayag, Caroline E. Haldin, Nicola J. Corbett, Karl J. Wahlin, Colleen Cowan, Sanja Turturro, Peter E. Larsen, Beatrix Kovacs, Dane P. Witmer, David Valle, Donald J. Zack, Daniel A. Nicholson, and Shunbin Xu. Inactivation of the microRNA-183/96/182 cluster results in syndromic retinal degeneration. *Proceedings of the National Academy of Sciences of the United States of America*, 110(6):E507–16, 2013. ISSN 1091-6490. doi: 10.1073/pnas.1212655110. URL http://www.pnas.org/cgi/content/long/110/6/E507.

Steven P. Lund, Dan Nettleton, Davis J. McCarthy, and Gordon K. Smyth. Detecting differential expression in RNA-sequence data using quasi-likelihood with shrunken dispersion estimates. *Statistical Applications in Genetics and Molecular Biology*, 11(5), 2012. ISSN 15446115. doi: 10.1515/1544-6115.1826.

Linda Madisen, Theresa A. Zwingman, Susan M. Sunkin, Seung Wook Oh, Hatim A. Zariwala, Hong Gu, Lydia L. Ng, Richard D. Palmiter, Michael J. Hawrylycz, Allan R. Jones, Ed S. Lein, and Hongkui Zeng. A robust and high-throughput Cre reporting and characterization system for the whole mouse brain. *Nature neuroscience*, 13 (1):133–40, 2010. ISSN 1546-1726. doi: 10.1038/nn.2467. URL http://www.ncbi.nlm.nih.gov/pubmed/20023653{%}5Cnhttp://www.pubmedcentral.nih.gov/articlerender.fcgi?artid=PMC2840225.

Davis J. McCarthy, Yunshun Chen, and Gordon K. Smyth. Differential expression analysis of multifactor RNA-Seq experiments with respect to biological variation. *Nucleic Acids Research*, 40(10):4288–4297, 2012. ISSN 03051048. doi: 10.1093/nar/gks042.

Alisa Mo, Chongyuan Luo, Fred P. Davis, Eran A. Mukamel, Gilbert L. Henry, Joseph R. Nery, Mark A. Urich, Serge Picard, Ryan Lister, Sean R. Eddy, Michael A. Beer, Joseph R. Ecker, and Jeremy Nathans. Epigenomic landscapes of retinal rods and cones. *eLife*, 5(MARCH2016), 2016. ISSN 2050084X. doi: 10.7554/eLife.11613.

Debarshi Mustafi, Andreas H. Engel, and Krzysztof Palczewski. Structure of Cone Photoreceptors Debarshi. *Ratio*, 28(4):289–302, 2009. ISSN 1946-6242. doi: 10.1124/dmd.107.016501.CYP3A4-Mediated.

Shuichi Obata and Jiro Usukura. Morphogenesis of the photoreeeptor outer segment during postnatal development in the mouse (BALB/c) retina. *Cell & Tissue Research*, pages 39–48, 1992.

John W. Olney. An Electron Microscopic Study of Synapse Formation, Receptor Outer Segment Development, and other Aspects of Developing Mouse Retina. *Investivative Ophthalmology*, 7(3):250–268, 1968.

Chin-tong Ong and Victor G. Corces. CTCF : an architectural protein bridging genome topology and function. *Nature Publishing Group*, 15(4):234–246, 2014. ISSN 1471-0056. doi: 10.1038/nrg3663. URL http://dx.doi.org/10.1038/nrg3663.

Ulrich Pfisterer, James Wood, Kristian Nihlberg, Oskar Hallgren, Leif Bjermer, Gunilla Westergren-Thorsson, Olle Lindvall, and Malin Parmar. Efficient induction of functional neurons from adult human fibroblasts. *Cell Cycle*, 10(19): 3311–3316, 2011. ISSN 15384101. doi: 10.4161/cc.10.19.17584.

Jennifer E. Phillips and Victor G. Corces. CTCF: Master Weaver of the Genome. *Cell*, 137(7):1194–1211, 2009. ISSN 00928674. doi: 10.1016/j.cell.2009.06.001.

Claudio Punzo, Karl Kornacker, and Constance L. Cepko. Stimulation of the insulin/mTOR pathway delays cone death in a mouse model of retinitis pigmentosa. *Nature Neuroscience*, 12(1):44–52, 2009. ISSN 1097-6256. doi: 10.1038/nn.2234. URL http://www.pubmedcentral.nih.gov/articlerender.fcgi?artid=3339764{&}tool=pmcentrez{&}rendertype=abstract{%}5Cnhttp://www.nature.com/doifinder/10.1038/nn.2234.

José-Alain Sahel and Botond Roska. Gene Therapy for Blindness. *Annu. Rev. Neurosci*, 36:467–88, 2013. ISSN 0147-006X. doi: 10.1146/annurev-neuro-062012-170304.

Rikako Sanuki, Akishi Onishi, Chieko Koike, Rieko Muramatsu, Satoshi Watanabe, Yuki Muranishi, Shoichi Irie, Shinji Uneo, Toshiyuki Koyasu, Ryosuke Matsui, Yoan Chérasse, Yoshihiro Urade, Dai Watanabe, Mineo Kondo, Toshihide Yamashita, and Takahisa Furukawa. miR-124a is required for hippocampal axogenesis and retinal cone survival through Lhx2 suppression. *Nature neuroscience*, 14(9):1125–1134, 2011. ISSN 1097-6256. doi: 10.1038/nn.2897. URL http://dx.doi.org/10.1038/nn.2897.

Shinya Satoh, Ke Tang, Atsumi Iida, Mariko Inoue, Tatsuhiko Kodama, Sophia Y Tsai, Ming-Jer Tsai, Yasuhide Furuta, and Sumiko Watanabe. The spatial patterning of mouse cone opsin expression is regulated by bone morphogenetic protein signaling through downstream effector COUP-TF nuclear receptors. *The Journal of neuroscience : the official journal of the Society for Neuroscience*, 29(40):12401–11, 2009. ISSN 1529-2401. doi: 10.1523/JNEUROSCI.0951-09.2009. URL http://www.pubmedcentral.nih.gov/articlerender.fcgi?artid=2791207{&}tool=pmcentrez{&}rendertype=abstract.

Tina Sedmak and Uwe Wolfrum. Intraflagellar transport proteins in ciliogenesis of photoreceptor cells. *Biology of the cell / under the auspices of the European Cell Biology Organization*, 103(10):449–466, 2011. ISSN 1768-322X. doi: 10.1042/BC20110034.

Sandra Siegert, Brigitte Gross Scherf, Karina Del Punta, Nick Didkovsky, Nathaniel Heintz, and Botond Roska. Genetic address book for retinal cell types. *Nature Neuroscience*, 12(9):1197–1204, 2009. ISSN 1097-6256. doi: 10.1038/nn.2370. URL http://dx.doi.org/10.1038/nn.2370.

Sandra Siegert, Eric Cabuy, Brigitte Gross Scherf, Hubertus Kohler, Satchidananda Panda, Yun-Zheng Le, Hans J. Fehling, Dimos Gaidatzis, Michael B. Stadler, and Botond Roska. Transcriptional code and disease map for adult retinal cell types. *Nat Neurosci*, 15(3):487–95, S1–2, 2012. ISSN 1097-6256. doi: 10.1038/nn.3032. URL http://www.ncbi.nlm.nih.gov/pubmed/22267162.

Esther Y. Son, Justin K. Ichida, Brian J. Wainger, Jeremy S. Toma, Victor F. Rafuse, Clifford J. Woolf, and Kevin Eggan. Conversion of mouse and human fibroblasts into functional spinal motor neurons. *Cell Stem Cell*, 9(3):205–218, 2011. ISSN 19345909. doi: 10.1016/j.stem.2011.07.014. URL http://dx.doi.org/10.1016/j.stem.2011.07.014.

Bryce L. Sopher, Paula D. Ladd, Victor V. Pineda, Randell T. Libby, M. Susan, James B. Hurley, Cortlandt P. Thienes, Terry Gaasterland, N. Filippova, Galina, and Albert R. La Spada. CTCF regulates ataxin-7 expression through promotion of a convergently transcribed, antisense non-coding RNA. *Neuron*, 70(6):1071–1084, 2012. doi: 10.1016/j.neuron.2011.05.027.CTCF.

Garrett A. Soukup. Little but loud: Small RNAs have a resounding affect on ear development, 2009. ISSN 00068993.

Guilford Street and London Wcn. Motile and non-motile cilia in human pathology: from function to phenotypes. *The Journal of Pathology*, 2016. doi: 10.1002/path.4843.

Thomas R. Sundermeier and Krzysztof Palczewski. The physiological impact of microRNA gene regulation in the retina, 2012. ISSN 1420682X.

Anand Swaroop, Douglas Kim, and Douglas Forrest. Transcriptional regulation of photoreceptor development and homeostasis in the mammalian retina. *Nature reviews. Neuroscience*, 11(8):563–576, 2010. ISSN 1471-003X. doi: 10.1038/nrn2880. URL http://dx.doi.org/10.1038/nrn2880.

Thomas Vierbuchen, Austin Ostermeier, Zhiping P. Pang, Yuko Kokubu, Thomas C. Suedhof, and Marius Wernig. Direct conversion of fibroblasts to functional neurons by defined factors. *Nature*, 463:1035–1042, 2010. ISSN 18788750. doi: 10.1016/j.wneu.2011.11.002.

Sui Wang and Constance L. Cepko. Photoreceptor fate determination in the vertebrate retina. *Investigative Ophthalmology and Visual Science*, 57(5):ORSFe1–ORSFe6, 2016. ISSN 15525783. doi: 10.1167/iovs.15-17672.

Frank S. Werblin. The retinal hypercircuit: a repeating synaptic interactive motif underlying visual function. *The Journal of physiology*, 589(Pt 15):3691–3702, 2011. ISSN 1469-7793. doi: jphysiol.2011.210617[pii]\r10.1113/jphysiol.2011.210617.

Gabrielle Wheway, David A. Parry, and Colin A. Johnson. The role of primary cilia in the development and disease of the retina. *Organogenesis*, 10(1):69–85, 2014. ISSN 1555-8592. doi: 10.4161/org.26710. URL http://www.pubmedcentral.nih.gov/articlerender.fcgi?artid=4049897{&}tool=pmcentrez{&}rendertype=abstract.

Kenneth C. Wikler, Agoston Szel, and Anne Lise Jacobsen. Positional information and opsin identity in retinal cones. *Journal of Comparative Neurology*, 374(1):

96–107, 1996. ISSN 00219967. doi: 10.1002/(SICI)1096-9861(19961007)374:1<96::AID-CNE7>3.0.CO;2-I.

Shunbin Xu, P. Dane Witmer, Stephen Lumayag, Beatrix Kovacs, and David Valle. MicroRNA (miRNA) transcriptome of mouse retina and identification of a sensory organ-specific miRNA cluster. *Journal of Biological Chemistry*, 282 (34):25053–25066, 2007. ISSN 00219258. doi: 10.1074/jbc.M700501200.

Rui Yi, H Amalia Pasolli, Markus Landthaler, Markus Hafner, Tolulope Ojo, Robert Sheridan, Chris Sander, Donal O'Carroll, Markus Stoffel, Thomas Tuschl, Elaine Fuchs, Donal O 'carroll, Markus Stoffel, Thomas Tuschl, and Elaine Fuchs. DGCR8-dependent microRNA biogenesis is essential for skin development. *Proceedings of the National Academy of Sciences of the United States of America*, 106(2):498–502, 2009. ISSN 1091-6490. doi: 10.1073/pnas.0810766105. URL http://www.ncbi.nlm.nih.gov/pubmed/19114655.

Seung Yun Yoo, Mark E. Pennesi, Edwin J. Weeber, Bisong Xu, Richard Atkinson, Shiming Chen, Dawna L. Armstrong, Samuel M. Wu, J. David Sweatt, and Huda Y. Zoghbi. SCA7 knockin mice model human SCA7 and reveal gradual accumulation of mutant ataxin-7 in neurons and abnormalities in short-term plasticity. *Neuron*, 37(3):383–401, 2003. ISSN 08966273. doi: 10.1016/S0896-6273(02)01190-X.

Ling-li Zhang, Hemal R. Pathak, Douglas A. Coulter, Michael A. Freed, Noga Vardi, and A. Michael. Shift of Intracellular Chloride Concentration in Ganglion and Amacrine Cells of Developing Mouse Retina. *Journal of Neurophysiology*, 95:2404–2416, 2006. doi: 10.1152/jn.00578.2005.

Yingsha Zhang, Chang Hui Pak, Yan Han, Henrik Ahlenius, Zhenjie Zhang, Soham Chanda, Samuele Marro, Christopher Patzke, Claudio Acuna, Jason Covy, Wei Xu, Nan Yang, Tamas Danko, Lu Chen, Marius Wernig, and Thomas C. Südhof. Rapid single-step induction of functional neurons from human pluripotent stem cells. *Neuron*, 78(5):785–798, 2013. ISSN 08966273. doi: 10.1016/j.neuron.2013.05.029.

Yong Zhang, Tao Liu, Clifford A. Meyer, Jérôme Eeckhoute, David S. Johnson, Bradley E. Bernstein, Chad Nussbaum, Richard M. Myers, Myles Brown, Wei Li, and X. Shirley Liu. Model-based Analysis of ChIP-Seq (MACS). *Genome Biology*, 9(9):R137, 2008. ISSN 1465-6906. doi: 10.1186/gb-2008-9-9-r137. URL http://genomebiology.biomedcentral.com/articles/10.1186/gb-2008-9-9-r137.

Qubo Zhu, Wenyu Sun, Kiichiro Okano, Yu Chen, Ning Zhang, Tadao Maeda, and Krzysztof Palczewski. Sponge transgenic mouse model reveals important roles for the MicroRNA-183 (miR-183)/96/182 cluster in postmitotic photoreceptors of the retina. *Journal of Biological Chemistry*, 286(36):31749–31760, 2011. ISSN 00219258. doi: 10.1074/jbc.M111.259028.